

DISTANCE-DEPENDENCE OF PLASMON-MULTIEXCITON COUPLING  
BETWEEN CDSE QUANTUM DOTS AND GOLD NANOSTRUCTURES

by

Jose Fernando Castaneda

A thesis submitted to the faculty of  
The University of North Carolina at Charlotte  
in partial fulfillment of the requirements  
for the degree of Master of Science in  
Chemistry

Charlotte

2015

Approved by:

---

Dr. Marcus Jones

---

Dr. Tsing-Hua Her

---

Dr. Juan Luis Vivero-Escoto

---

Dr. Michael G. Walter

©2015  
Jose Fernando Castaneda  
ALL RIGHTS RESERVED

## ABSTRACT

JOSE FERNANDO CASTANEDA. Distance-dependence of plasmon-multiexciton coupling between cdse quantum dots and gold nanostructures. (Under the direction of Dr. MARCUS JONES)

Quantum confinement that semiconductors experience at the nanoscale facilitate the creation of multiexcitons. However, this same confinement also increases the efficiency of Auger recombination which result in low quantum yields from these states. The emission rates of quantum dots are known to be modified by the surface plasmon resonances of gold nanostructures. This plasmon-exciton interaction is thought to be a near-field interaction between the quantum dot excited state and the plasmon resonance of the metal, thus, indicating an interaction that is distance-dependant. A similar interaction is expected between the quantum dot multiexciton state and the plasmon resonance of the metal.

In this work, the distance-dependence of the plasmon-multiexciton interaction was probed by use of modified substrates that controlled separation between gold nanoparticles and quantum dots through the use of bifunctional molecules, layer-by-layer deposition, and single molecule fluorescence techniques.

## TABLE OF CONTENTS

CHAPTER 1:	INTRODUCTION	1
1.1	Photovoltaic Systems	1
1.2	Quantum Dots	2
1.3	Multiexcitons in Quantum Dots	3
1.4	Auger Recombination Limitation	5
CHAPTER 2:	METAL ENHANCED FLUORESCENCE	7
2.1	Drexhage Experiment	7
2.2	Optical Properties of Metals	8
2.3	Plasmon-Exciton Coupling	9
2.4	Plasmon-Multiexciton Coupling	11
2.5	Sample Structure for Controlled Plasmon-Multiexciton Coupling	14
CHAPTER 3:	EXPERIMENTAL	17
3.1	Gold Nanoparticle Synthesis	17
3.2	Gold Nanoparticle Film Formation	17
3.3	Spin-Assisted Layer-by-Layer Deposition	18
3.4	Single Molecule Spectroscopy	20
3.4.1	Laser System Setup	20
3.4.2	Single Particle Imaging	21
3.4.3	Time Correlated Single Photon Counting	21
3.4.4	Time Tagged Time Resolved Mode	22
3.4.5	Photon Correlation	22

CHAPTER 4: RESULTS AND DISCUSSION	23
4.1 Gold Nanoparticles	23
4.2 Gold Nanoparticle Film	25
4.3 Polyelectrolyte Spacer Layer	31
4.4 Single Molecule Spectroscopy	37
4.4.1 Plasmon-Exciton Coupling	41
4.4.2 Plasmon-Multiexciton Coupling	54
CHAPTER 5: CONCLUSIONS	67
REFERENCES	69

## CHAPTER 1: INTRODUCTION

### 1.1 Photovoltaic Systems

The need for carbon-free energy is constantly growing as the finite supply of fossil fuels are slowly being depleted. The ability to harness energy from the sun is viewed as one of the most promising routes to decrease this dependence as a large percentage of the solar radiation that penetrates the earth's atmosphere is in the visible range. As a result research in photovoltaics has risen dramatically in search of ways to efficiently convert this energy from the sun into useful work.

In a solar cell, a photon from the sun can create an electron-hole pair or exciton in a light absorbing material, and these charge carriers are pulled away from each other creating a current. Semiconductors are seen as prime candidates for producing these charge carriers as these materials absorb energy in the visible range and can efficiently produce excitons. At the moment the best commercial single p-n junction solar cells consist of silicon. These systems can theoretically reach the Shockley/Queisser maximum efficiency limit of 30%.<sup>1</sup> Losses result for several reasons: (i) photons with energies below the bandgap energy cannot be absorbed, (ii) photons with energies above the bandgap energy will lose the excess energy as heat due to carrier relaxation, (iii) thermodynamic losses result from the chemical potential output from thermalized excited

states being less than the bandgap energy, (iv) and radiative recombination of the exciton can also occur.<sup>2</sup> Systems with multiple light absorbers have gathered attention to reduce losses resulting from photons less than and above the bandgap energy. However, an alternative method of utilizing excess energy would be to produce an additional exciton within the same material in a process known as impact ionization.

Impact ionization occurs in a material when a highly excited charge carrier is created and instead of phonon-assisted relaxation to the band edge excess energy is lost by creating an additional excited charge carrier. In bulk materials this process is inefficient as impact ionization competes with the faster intraband relaxation and requires incident photon energies at least many times the bandgap energy. However, in systems where charge carriers are confined to spaces comparable to or smaller than the Bohr exciton radius of that material, relaxation rates can be reduced and the impact ionization process can be enhanced.<sup>3</sup> Such systems that contain materials that can efficiently create multiple excitons per photon can theoretically reach a maximum efficiency limit of 44.4%, a relative 48% increase from the Shockley/Queisser limit.<sup>2</sup>

## 1.2 Quantum Dots

When semiconductors absorb a photon of higher energy or equal to the bandgap energy an exciton is created. This bandgap energy is intrinsic to the material, but when size dimensions are comparable to the Bohr exciton radius this energy is no longer fixed. The Bohr exciton radius is the allowed spatial distance that the electron-hole pair can be separated in the bulk, and for most materials is below 10 nm.<sup>4</sup> In this size regime, the semiconductor experiences adjustment of its electronic transitions resulting from the smaller physical dimensions, otherwise known as quantum confinement.

In the bulk, states are closely spaced resulting in continuous bands, whereas at the nanoscale, are farther apart in energy resulting in atomic-like states. As the physical dimensions decrease a blue shift occurs in the energy spectrum of the material as well. Therefore, semiconductor nanocrystals or quantum dots display tunable optical properties, as the bandgap energy can be adjusted accordingly by size.

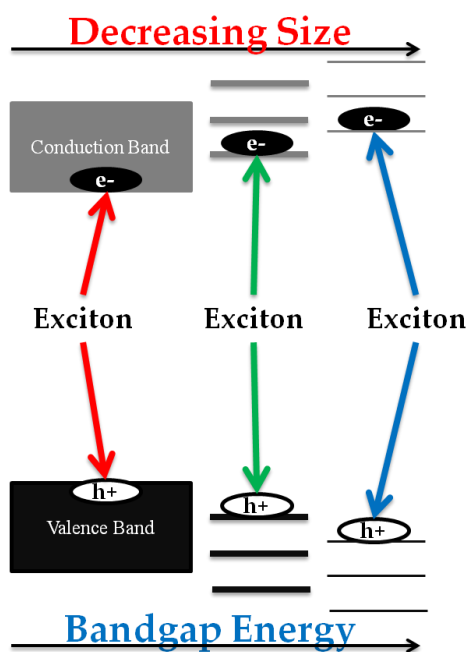


Figure 1: Semiconductor band structure at the bulk and nanoscale

Figure 1 illustrates the band structure of a semiconductor as the size of the material decreases. From left to right the bandgap energy increases and the states become more discrete. It is from this quantization of the band structure that relaxation rates are decreased as states are farther apart in energy.<sup>3</sup>

### 1.3 Multiexcitons in Quantum Dots

Efficient impact ionization was first measured in quantum dots by Schaller and Klimov in 2004.<sup>5</sup> Transient absorption was used to probe the multiexciton and single

exciton relaxation dynamics in PbSe materials as the two processes differ. Single exciton recombination occurred on the submicrosecond time frame, where as multiexcitons recombined on the picosecond time frame via Auger recombination. Auger recombination can be thought as the reverse impact ionization process. In impact ionization a highly energetic charge carrier relaxes through energy transfer to create an additional exciton. However, the Auger process occurs when multiple excitons have been created and an exciton would relax through energy transfer to a remaining charge carrier. These two processes are shown in Figure 2 below.

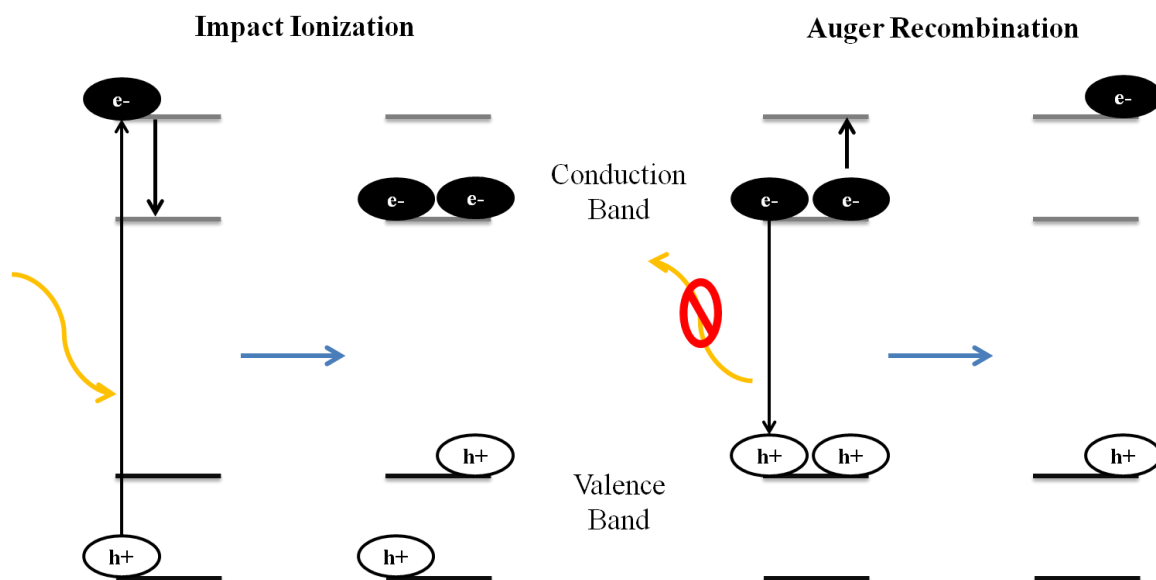


Figure 2: Impact ionization vs. Auger recombination

Schaller and Klimov demonstrated the creation of multiexcitons by impact ionization through excitation with a single photon  $\sim 3.6$  times the bandgap energy, but they also showed that multiexcitons could be created by low energy high excitation densities as well. In this picture multiexcitons are created by sequential absorption of photons. Figure 3 demonstrates the two methods of how multiexcitons can be created.

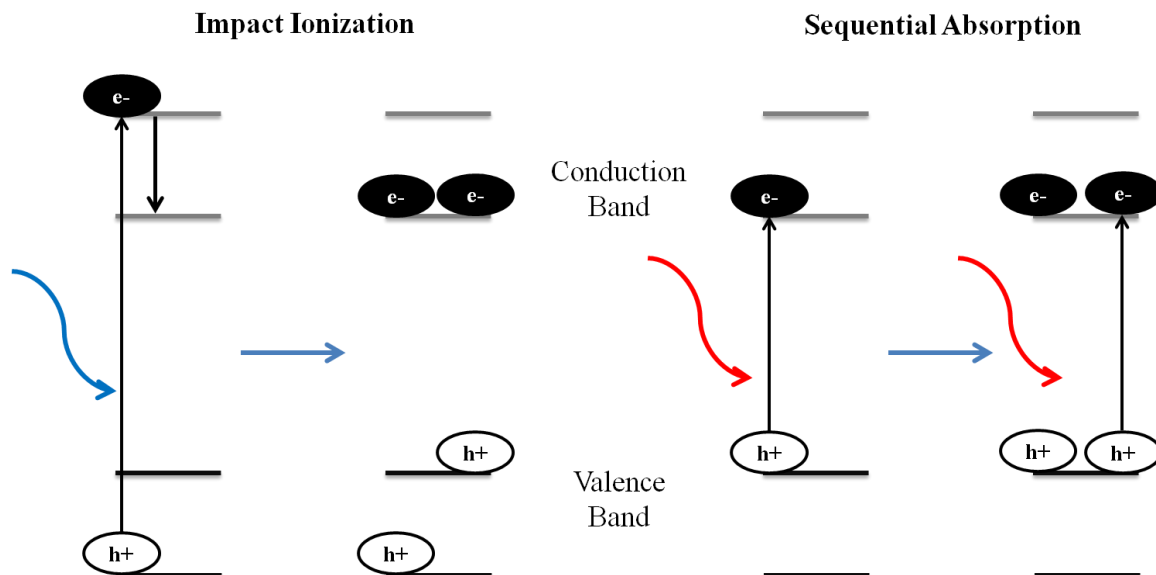


Figure 3: Possible methods for creation of multiexcitons

As shown in Figure 3 impact ionization occurs through absorption of a high energy photon resulting in two excitons being formed. Multiexcitons can also be formed through sequential adsorption of photons having at least the same energy as the bandgap energy.

#### 1.4 Auger Recombination Limitation

As mentioned earlier, materials with the ability to efficiently create multiexcitons have obvious solar applications. For example, Sambur et al. incorporated PbS quantum dots in dye-sensitized solar cells that demonstrated absorbed photon-to-current efficiencies above 100%.<sup>6</sup> In an ideal system each absorbed photon would contribute to current at an efficiency of 100%. An efficiency over 100% can be interpreted as for each absorbed photon more than one carrier contributed to current. This ability to create multiexcitons has also viewed quantum dots as potential materials for light-emitting devices that require emission from higher-order excitons.<sup>7,8,9,10,11</sup> Potential applications have also been seen in quantum computing.<sup>12,13,14</sup> However, a major hindrance to all of these applications is the non-radiative Auger recombination process.

All quantum confined systems undergo the Auger process due to the enhanced wavefunction overlap between electrons and holes, which result in stronger carrier-carrier coulombic interactions. It would then be expected in smaller (higher energy) nanocrystals Auger recombination would be enhanced due to these enhanced coulombic interactions and the increased overlap of the electron and hole wavefunctions, thus limiting the size tunable properties for potential applications. Schaller and Klimov also demonstrated this relationship between the Auger recombination rate and nanocrystal size by their early transient absorption experiments, which reported that the Auger relaxation rate correlates linearly with the nanocrystal size.<sup>5</sup>

Several methods have been reported to reduce the Auger process. Such methods include applying shells of a different material or different geometries like rods.<sup>15,10,16,17,18</sup> These methods have demonstrated that the Auger mechanism can be modified, but suffer from inhomogeneity within samples with current synthetic methods. For example, in the work by Park et al. CdSe quantum dots demonstrated a max biexciton quantum yield of ~0.9 when a large CdS shell was applied, however, quantum yields varied greatly within samples which was attributed to inhomogeneous shell structures and core-shell interfaces.<sup>18</sup>

## CHAPTER 2: METAL ENHANCED FLUORESCENCE

### 2.1 Drexhage Experiment

Metals have long been known to modify emission from fluorescent materials. Drexhage was the first to report modified emission from a dye molecule in the presence of a metal.<sup>19</sup> In his experiments europium-dibenzoylmethane complex molecules were placed at known distances from a silver mirror. His results demonstrated an oscillatory nature of the fluorescence lifetime as a function of distance between the dye and the silver mirror.

Drexhage was able to simulate the interaction between the molecule and the mirror, which agreed fairly well with experimental results. His model consisted of reflected emitted radiation that was either constructively or destructively interfering with radiation emitted directly at the molecule. The constructive or destructive nature oscillated as a function of distance, and at distances where constructive interference occurred the radiated power was enhanced while a shorter fluorescence lifetime was measured. Likewise, at distances where destructive interference occurred the radiated power was reduced while measuring a longer fluorescence lifetime. This model agreed quite well with experimental data except at very small distances between the molecule and the metal, where both the radiated power and fluorescence lifetime were reduced. Despite this discrepancy it was shown that metals can modify the local environment of fluorophores, which resulted in modified properties.

## 2.2 Optical Properties of Metals

When discussing how metals interact with light their optical properties must be considered. The valence electrons of metals are often considered to be "free", where their wavefunctions are delocalized among several nuclei. Upon applying an electromagnetic field of a certain frequency, polarization of these free electrons with respect to their ionic nuclei induces a net charge difference that generates a restoring force, which causes the electrons to oscillate in resonance with the applied field. This collective oscillation is known as a plasmon resonance, and since these oscillations involve charges (electrons) induced fields are produced which can alter the surroundings.

Light-metals interactions are described by their complex dielectric constant and refractive index, which are both functions of applied field frequency. Electron motion with an applied field can be modeled as a damped oscillator with an external driving force. The dielectric function ( $\epsilon_m$ ) of a metal can then be expressed as:

$$\epsilon_m = 1 - \frac{\omega_p^2}{(\omega^2 + \gamma^2)} + \frac{i\omega_p^2\gamma}{\omega(\omega^2 + \gamma^2)} \quad (1)$$

where  $\omega$  is the applied field frequency,  $\omega_p$  the plasmon frequency of the metal, and  $\gamma$  the damping constant. The damping constant ( $\gamma$ ) arises from electron-electron, electron-phonon, and electron-defect scattering and can be considered small for the bulk, which allows the dielectric function to be expressed as the Drude result.<sup>20</sup>

$$\epsilon_m = 1 - \frac{\omega_p^2}{\omega^2} \quad (2)$$

The Drude result can describe metals at the bulk level fairly well, however, when size dimensions become smaller than the mean free path of electrons a new electron-surface

scattering component contributes to the damping constant ( $\gamma$ ) resulting in the term no longer being negligible.

In these smaller dimensions the resonance is often referred to as a surface plasmon resonance as interactions are now expected to be with the surface of the metal. The resonance condition is also now dependent on shape, size, and both dielectric constants of the metal and the surrounding medium.<sup>21</sup> As the surface geometry changes with size and shape a shift in the electric field density on the surface causes a change in the oscillation frequency of the electrons. Also, changing the dielectric constant of the surrounding medium will affect the oscillation frequency because of the varying ability to accommodate electron charge density on the surface. Figure 4 demonstrates a surface plasmon resonance occurring in a nanoparticle, which modifies the surrounding with induced fields.

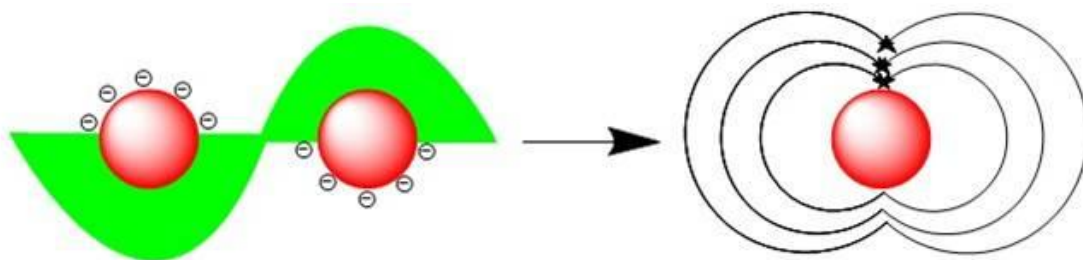


Figure 4: Surface plasmon resonance of a nanoparticle

### 2.3 Plasmon-Exciton Coupling

Plasmon-exciton coupling is used to describe the interaction between metal and semiconductor nanosystems, and is thought to be a near-field interaction between the semiconductor exciton state and the surface plasmon resonance of the metal, indicating an interaction that is distance-dependent.<sup>22</sup> This would also indicate that largest effects occur when the exciton state and plasmon frequencies are in resonance.<sup>23</sup> The oscillating

near field of the emitter is thought to generate a localized surface plasmon resonance in a nearby metal nanostructure. Most efficiently in the resonant case, energy is then transferred from the emitter to the metal and the system radiates.<sup>22,24</sup> As a result increased fluorescence quantum yields and decreased fluorescence lifetimes are measured.<sup>25,26,27,28,29,30,16,31</sup> These results can be explained by introduction of a fast radiative process by the metal.<sup>22,32</sup>

Spontaneous emission is often described to occur through excited atoms interacting with vacuum fluctuations. It is also known that spontaneous emission depends strongly on the local environment. This was exploited by Purcell in 1946.<sup>33</sup> His experiments demonstrated that an atom placed in a cavity can radiate faster through interactions with its own far-field than an atom in free space.

In free-space emission the fluorescence quantum yields ( $\Phi$ ) and lifetimes ( $T$ ) are dominated by non-radiative processes ( $K_{nr}$ ).

$$\Phi = \frac{\Gamma}{\Gamma + K_{nr}} \quad (3)$$

$$T = \frac{1}{\Gamma + K_{nr}} \quad (4)$$

The radiative rate ( $\Gamma$ ) is normally intrinsic to the material so it can be seen that both the quantum yield and lifetime change in the same matter. Either they both increase or both decrease. However, if a radiative process ( $\Gamma_m$ ) is introduced by the presence of a metal both the now modified quantum yield ( $\Phi_m$ ) and fluorescence lifetime ( $T_m$ ) give different results.

$$\Phi_m = \frac{\Gamma + \Gamma_m}{\Gamma + \Gamma_m + K_{nr}} \quad (5)$$

$$T_m = \frac{1}{\Gamma + \Gamma_m + K_{nr}} \quad (6)$$

As it can be seen in the presence of a metal the quantum yield increases while the fluorescence lifetime decreases.

Plasmon-exciton coupling also modifies phenomena present at the single emitter level. Single quantum dots display fluorescence intermittency or blinking, which is thought to occur through a fast Auger-type process. In this process an exciton would recombine resulting in energy transfer to another carrier, which at this time is considered to be in a non-emissive off state. This process differs from Auger recombination seen in multiexcitons as the nanocrystal has become charged by a carrier trapped on the surface or ejected completely out of the nanocrystal, resulting in an electron or hole present at the moment of excitation. Upon excitation a three particle system or trion is formed, which non-radiatively recombines on the order of picoseconds just like the Auger process seen for multiexcitons. It is not until the carrier ejected or trapped on the surface returns within the nanocrystal that an on state can be reached again.<sup>34,35</sup> However, in the presence of a metal gray states can arise as well as the suppression of blinking. Gray states are thought to be low emitting states attributed to the emission from charged quantum dots, where the radiative recombination of a charged quantum dot has been enhanced to a point where it can compete with the non-radiative process normally associated with charged particles.<sup>30,23</sup>

#### 2.4 Plasmon-Multiexciton Coupling

The surface plasmon resonances of metals can modify multiexciton emission in similar ways demonstrated for single exciton emission. However, measuring multiexciton

emission is not trivial. Quantum yields from these states are normally low since Auger recombination is the dominant process, and certain instrumentation is needed.

Photon-correlation measurements using the Hanbury-Brown Twiss geometry can measure multiexciton emission in a single emitter as this method operates on the same concepts of time-correlated single photon counting and utilizes a 50/50 beam splitter that splits fluorescence so half the signal reaches two different detectors. Each detector is designated as start or stop, and time delays are measured for each start-stop process. Correlated histograms obtained can determine whether an emitter is displaying bunching behavior, where multiple photons are being detected within the same pulse period.<sup>12</sup>

Masuo et al. demonstrated enhancement of multiexciton emission from CdSe/ZnS quantum dots in the presence of silver nanoparticles.<sup>36</sup> His samples consisted of the nanocrystals embedded in a ~25 nm poly(methyl methacrylate) film with silver nanoparticles ranging from 30 nm - 100 nm in size drop-casted on top. Enhanced fluorescence intensities, reduced fluorescence lifetimes, and suppressed blinking were all reported in the presence of the silver nanoparticles, which are all results seen in plasmon-exciton coupling. However, photon correlation measurements also indicated increased bunching behavior as well, indicating there was enhancement of the multiexciton emission process as well. It was also reported much like plasmon-exciton coupling this interaction appears to be distance-dependent as varying coupling strengths were measured from nanocrystal to nanocrystal. These variations were attributed to the random distribution of the nanocrystals within the polymer film, which result in random distances from the silver nanoparticles.

In similar work by Leblanc et al. multiexciton emission was enhanced in the presence of a rough gold film sputtered onto a ~100 nm poly(methyl methacrylate)/CdSe/ZnS film.<sup>37</sup> Varying coupling strengths were also observed as well due to the large polymer thickness. However, increased fluorescence intensities and suppressed blinking were not observed. This was attributed to the possible competing non-radiative energy transfer to the chromium layer that was deposited under the polymer film, as metals are also known to quench fluorescence at small distances.<sup>38,39,40, 22, 41, 27,32,</sup>  
<sup>42</sup> However, neither work displayed where the surface plasmon resonances occurred relative to the quantum dot exciton state. Masuo et al. also did not rule out the possibility of a nanocrystal being excited, emitting, excited, and reemitting within the same pulse period as the fast radiative components measured where on the order of the instrument response.

Naiki et al. further improved on the work with silver nanoparticles done by Masuo et al. to address issues stated earlier.<sup>43</sup> In similar fashion CdSe/ZnS nanocrystals were embedded in a ~25 nm poly(methyl methacrylate) film with silver nanoparticles 20 nm - 140 nm in size drop-casted on top. Femtosecond-pulsed laser excitation at 411 nm with ~200 fs pulse widths was used to eliminate the possibility of the excitation and emission process occurring twice within the same pulse period as first alluded to by Masuo et al. The spectral overlap between the surface plasmon resonances of the silver and the exciton state of the nanocrystals was also determined.

Results obtained were nearly identical to the previous work by Masuo et al as the excited state lifetimes decreased, fluorescence intensities increased, blinking was suppressed, and bunching behavior were all seen. Samples were excited at different

powers to study the power dependence with and without the presence of the silver nanoparticles. Samples with no silver demonstrated no multiexciton emission even at high power, but in the presence of the metal, samples demonstrated high multiexciton emission even at low power. This was attributed to the enhanced absorption that occurs by the electromagnetic fields created by the localized surface plasmon resonance upon direct excitation by the laser.

## 2.5 Sample Structure for Controlled Plasmon-Multiexciton Coupling

Several trends seem apparent regarding multiexciton emission mediated by the plasmon resonance in metal structures. Similar to the plasmon-exciton interaction, the process appears to be distance-dependent. In order to compete with the Auger recombination process the multiexciton emission rate must be enhanced, which is strongly correlated to the spectral overlap between the multiexciton state and the surface plasmon resonance.

Reported work all observed variability within samples due to a distribution of distances (coupling) between the semiconductor and metal nanostructures. To probe the distance-dependence of the plasmon-multiexciton interaction the following sample platform consisting of a polyelectrolyte polymer spacer between a gold nanostructured film and quantum dots was constructed as shown in figure 5.

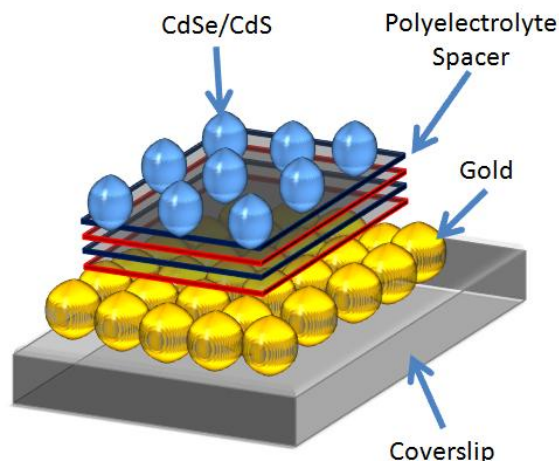


Figure 5: Sample platform for controlled distance between gold and semiconductors

Wet chemical synthetic methods have evolved that various shapes such as nanoparticles and nanorods can be easily made, each with different surface plasmon resonances arising from shape and size.<sup>21</sup> These nanostructures could be made into a film with the use of bifunctional silane molecules as linkers to the substrate.<sup>44,45,46,47,48</sup> Thus, films consisting of such nanostructures could be formed to obtain surface plasmon resonances at the desired energy. Such films produced in this manner have also been reported to be coated with silver shells, which would allow additional tuning of the surface plasmon frequency, or made conductive as well.<sup>49,44,50,51</sup>

For the work conducted here gold nanoparticles were synthesized by the reduction of tetrachloroauric acid with trisodium citrate, which was first introduced by Turkevich et al. in 1951, resulting nanoparticles have a negative surface charge due to citrate ions being absorbed on the particle surface.<sup>52,53</sup> Upon this negatively charged film polyelectrolytes can be deposited to form a spacer layer as demonstrated in the work by Kulakovich et al.<sup>25</sup> In this work gold nanoparticle films and CdSe/ZnS quantum dots were separated by positively charged poly(diallyldimethylammonium chloride) and negatively charged poly(sodium 4-styrenesulfonate) deposited using layer-by-layer

techniques. The polyelectrolyte spacer thickness was varied on top of the gold nanoparticle film and the quantum dots were drop-casted on top. Ensemble fluorescence measurements concluded a maximum enhancement at a 11.7 nm spacer thickness. Along with this work by Kulakovich et al. the use of the layer-by-layer technique has been reported on different types of gold surfaces.<sup>54,55,56,57,58,59</sup>

Layer-by-layer deposition offers the ability that the spacer layer thickness can be adjusted by ionic strength, pH, and number of layers deposited. Multilayers are constructed by alternating adsorption of anionic and cationic polyelectrolytes from immersion in solution with rinsing steps in between.<sup>60,61,62,63,64</sup> However, this method can be combined with spin-casting to form multilayers in a timely manner as traditional layer-by-layer deposition is driven by diffusion to the substrate surface under the influence of the electrostatic interaction, which can take up to several minutes per layer. However, in the spin-assisted layer-by-layer assembly this process can be done within seconds.<sup>65,66,67,68,69</sup> This method provides the route to control the distance between the gold and semiconductor nanostructures. Completed samples with varying polyelectrolyte thicknesses along with single molecule spectroscopy methods could then be used to probe the multiexciton-plasmon interaction as a function of distance between the two materials.

## CHAPTER 3: EXPERIMENTAL

### 3.1 Gold Nanoparticle Synthesis

Gold nanoparticles were synthesized according to the methods by Grabar et al.<sup>45</sup> A solution of 0.02 g gold(III) chloride trihydrate in 59.0 mL of Milli-Q H<sub>2</sub>O was brought to a boil. Under rigorous stirring 0.07200 g sodium citrate tribasic in 6.0 mL of Milli-Q H<sub>2</sub>O was injected. Once the solution obtained a burgundy color the reaction was kept under heat for an additional ten minutes under stirring. Heat was removed and stirring continued for ten minutes, and left to cool to room temperature. Once to room temperature synthesized particles were stored at 2° C. Ultraviolet-visible spectroscopy was conducted using the Cary 500 UV-vis spectrophotometer with a wavelength range from 400- 800 nm, integration of 1 second, and increment of 2 nm to determine at what energy the surface plasmon resonance occurred along with an estimation of the size and concentration using methods conducted by Haiss et al.<sup>70</sup> Transmission Electron Microscopy images were also taken using the JEOL 2100 electron microscope and images were analyzed using the ImageJ software.<sup>71</sup>

### 3.2 Gold Nanoparticle Film Formation

Coverslips (18 x 18 mm, Ted Pella, INC) underwent a piranha bath consisting of 30 mL H<sub>2</sub>SO<sub>4</sub> and 10 mL H<sub>2</sub>O<sub>2</sub> (30%) heated at 85° C for an hour, and rinsed extensively with deionized water. Coverslips then underwent a standard clean 1 bath consisting of 50 mL deionized water, 10 mL NH<sub>4</sub>OH (29%), and 10 mL H<sub>2</sub>O<sub>2</sub> (30%) heated at 85° C for

an additional hour, and rinsed extensively with deionized water. Cleaned coverslips were then stored in methanol until needed.

Cleaned coverslips were functionalized by immersion into a 10 % V/V (3-mercaptopropyl)trimethoxysilane/toluene or a 1 % V/V (3-aminopropyl)trimethoxysilane/methanol solution for 24 hours. Loosely bound silane molecules were removed by sonication in fresh solvent for a minute, and immersed into Milli-Q H<sub>2</sub>O for 10 minutes prior to Gold nanoparticle film formation or stored in methanol until needed.

Functionalized coverslips were then immersed into the synthesized gold nanoparticle solution for varying amounts of times. Saturation, usually was achieved within 12-24 hours. Loosely bound nanoparticles were removed by sonication in fresh solvent for a minute, and films were stored in Milli-Q H<sub>2</sub>O until needed. Prior to polyelectrolyte deposition the gold on one side on the coverslip was wiped off with methanol. Ultraviolet-visible spectroscopy was conducted using the Cary 500 UV-vis spectrophotometer with a wavelength range from 400- 800 nm, integration of 1 second, and increment of 2 nm to determine at what energy the surface plasmon resonance occurred with the resulting nanoparticle film. Atomic Force Microscopy was used to measure surface roughness and particle size using Digital Instruments Veeco Metrology Group Dimension 3100 Atomic Force Microscope at a scan rate of 1.99 Hz with 256 samples/line.

### 3.3 Spin-Assisted Layer-by-Layer Deposition

Polyelectrolyte solutions (25.0 mL) were made at an approximate concentration of 10 mM calculated from the molar mass of the monomer unit, where 0.4996 g of

poly(sodium 4-styrenesulfonate) ( $M_w \sim 70,000$ ) and 72  $\mu\text{L}$  of poly(allylamine) ( $M_w \sim 65,000$ , 20 wt. % in  $\text{H}_2\text{O}$ , Sigma-Aldrich) were dissolved into Milli-Q  $\text{H}_2\text{O}$ . The poly(allylamine) solution was adjusted to a pH of 5.5 with 0.1 M HCl before reaching the total volume.

All spin-assisted layer-by-layer depositions were done using the Chemat KW-4A spin coater. Polymers (150 mL) were deposited in alternating fashion with a Speed I setting of 2,500 rpm for 2 seconds, and a Speed II setting of 3000 rpm for 20 seconds. A rinsing step consisting of 250 mL of Milli-Q  $\text{H}_2\text{O}$  being administered twice while the substrate was spinning with a Speed I setting at 2,500 rpm for 2 seconds and Speed II setting of 3,000 rpm for 30 seconds was conducted after each polymer deposition. Depositions were either conducted on freshly cleaned coverslips or gold nanoparticle films. Both surfaces are negatively charged so poly(allylamine) was deposited first and was also the last layer deposited before the drying step, which consisted of a rinsing step with increased time for Speed II to 60 seconds. This was followed by an additional drying step where no Milli-Q  $\text{H}_2\text{O}$  was administered while spinning and films were left to dry for an additional 24 hour period. Obtained polyelectrolyte films on coverslips were scratched using a custom made mask for a guide and Atomic force Microscopy was used to determine the step-edge thickness. Polyelectrolyte films on gold nanoparticle films were stored until needed for single molecule spectroscopy measurements, where a CdSe/CdS solution, which was obtained from Dr. Gretak's group at the University of South Carolina, was diluted by five orders of magnitude in toluene were spin-coated while the substrate was spinning with a Speed I setting of 600 rpm for 2 sec and a Speed II setting of 3,000 rpm for 30 seconds.

### 3.4 Single Molecule Spectroscopy

Single quantum dot emission was monitored using a homebuilt laser scanning confocal microscope as shown in Figure 6.

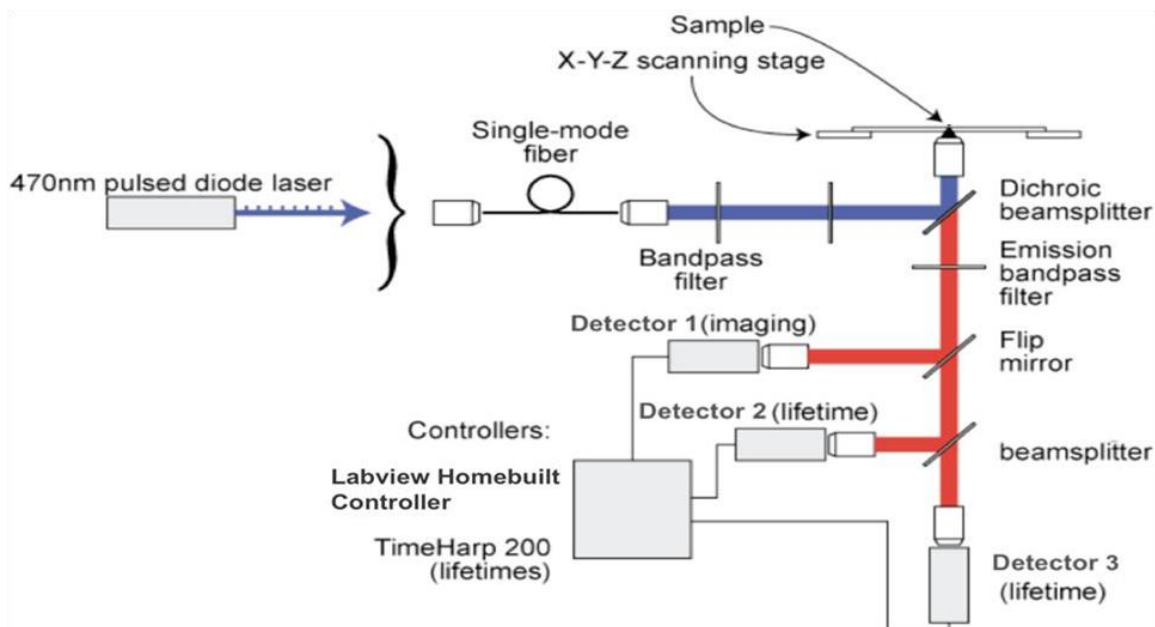


Figure 6: Single molecule spectroscopy setup

#### 3.4.1 Laser System Setup

A PicoQuant PDL 800-B pulsed diode laser with a LDH Series 470 nm laser head was used as the excitation source at a pulse repetition frequency of 10 MHz and 90 ps pulse width. The excitation pulses are couple to a single-mode optical fiber and collimated by a Nikon 10X objective lens and then pass through a bandpass filter with a bandwidth of 20 nm centered about 470 nm. Excitation pulses reach a 500 nm cutoff dichroic beamsplitter before reaching a Zeiss 100x 1.25 NA oil immersion objective lens that focuses the excitation beam onto the sample in an inverted geometry.

Samples sit on a Mad City Labs three dimensional nano-positioning system stage that can be adjusted in the x, y, and z, directions. Emission from the samples pass back

through the Zeiss objective lens through a bandpass filter with a 50 nm bandwidth centered about 605 nm then to a flip mirror. Depending on the orientation of this mirror, emission can be sent to a Melles Griot 160/0.17 objective lens that focuses the emission onto an EG & E Single Photon Counting Module for imaging or to a 50/50 beamsplitter that splits the signal between two Nikon 10X objective lenses that focus the emission onto PicoQuant PDM Series single photon avalanche photodiodes for single photon counting measurements. Signal from these single photon avalanche photodiodes are fed to the PicoQuant PRT 400 router then to the Time-Harp200 PCI Card.

### 3.4.2 Single Particle Imaging

Software used for imaging is a homebuilt LabVIEW program that can control the movement of the piezo scanning stage, and is capable of various scanning speeds and image pixel resolutions. This system enables the capability to image single particles within the full scan range of 75 x 75  $\mu\text{m}$  scan range down to a single pixel. All images were collected at 256 x 256 pixel resolution at 10 lines per second or at 512 x 512 pixel resolution at 5 lines per second.

### 3.4.3 Time Correlated Single Photon Counting

The Time-Harp200 PCI Card operates in reverse mode, where each detector after the 50/50 beamsplitter is designated as a start while the laser excitation pulses are the stop. The Time-Harp200 PCI Card correlates a histogram of the time delays for each start-stop process for each channel (detector) resulting in the capability of obtaining excited state fluorescence lifetime decays for single quantum dots. These fluorescence lifetime decays were collected for 30 seconds with a channel width of 30 ps. Obtained

decays were then fitted to a sum of exponentials in Igor Pro 6.35A5 to calculate excited state average lifetimes as well as emission lifetimes.

#### 3.4.4 Time Tagged Time Resolved Mode

In similar fashion to time correlated single photon counting, time delays are measured for each start-stop process which are considered as micro times, however an additional time tag is also assigned to each photon detected. This new time tag is relative to the beginning of the experiment generally known as the macro time. Now each detected photon has two time tags, the macro time and the micro time. Experiments conducted in time tagged time resolved mode were conducted for 30 seconds, and Igor Pro 6.35A5 was used to generate blinking traces from the macro times with 50 ms bin widths. These traces were then used to monitor the blinking dynamics of a single quantum dot.

#### 3.4.5 Photon Correlation

The Hanbury Brown-Twiss geometry can determine whether photons are correlated.<sup>72</sup> In this geometry the stop is no longer the laser excitation pulses. Signal is split between two detectors where one is designated as the start and the other the stop. In similar fashion to normal time correlated single photon counting, time delays are correlated into histograms, but are now centered about a time delay of zero. Photon correlation measurements were conducted for 120 seconds with a channel width of 240 ps. Average lifetimes were obtained from fitting obtained data to a sum of exponentials in Igor Pro 6.35A5.

## CHAPTER 4: RESULTS AND DISCUSSION

### 4.1 Gold Nanoparticles

Synthesized gold nanoparticles were characterized by UV-visible spectroscopy and transmission electron microscopy. Absorbance measurements determined the frequency of the surface plasmon resonance of the particles and can also be used to calculate the diameter and concentration using methods conducted by Haiss et al.<sup>70</sup>

$$Diameter (nm) = \exp\left(3.00 \frac{A_{spr}}{A_{450}} - 2.20\right) \quad (7)$$

The absorbance at the surface plasmon resonance maxima ( $A_{spr}$ ) and at 450 nm ( $A_{450}$ ) are easily obtained from spectra, however, transmission electron microscopy was also used to determine shape and diameter.

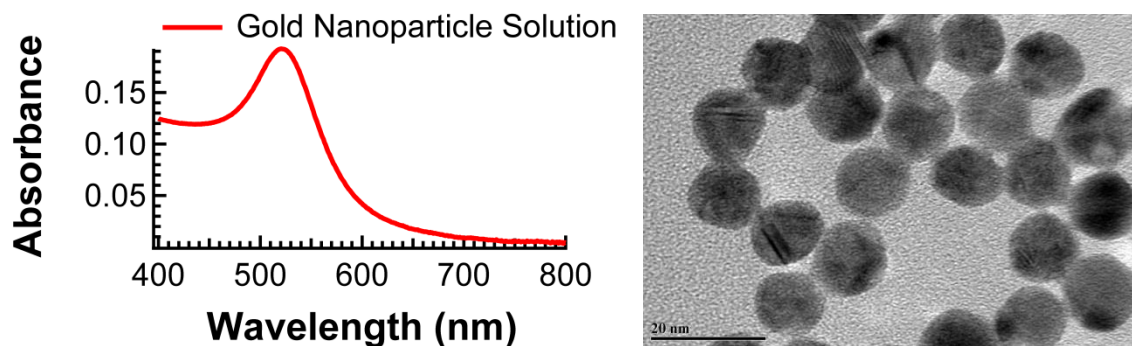


Figure 7: UV-Vis spectrum and TEM image of synthesized gold nanoparticles

Figure 7 shows typical absorbance and corresponding transmission electron microscopy image (300x magnification) of synthesized gold nanoparticles. Absorbance at

450 nm for the spectrum in Figure 4 measured a value of 0.12021 and the surface plasmon resonance maxima occurred at 521 nm with an absorbance value of 0.19236. These values along with equation (7) determined diameters of approximately 13.47 nm. Analysis of 73 particles by transmission electron microscopy determined diameters of  $11.70 \pm 1.53$  nm with the size distribution shown in Figure 8.

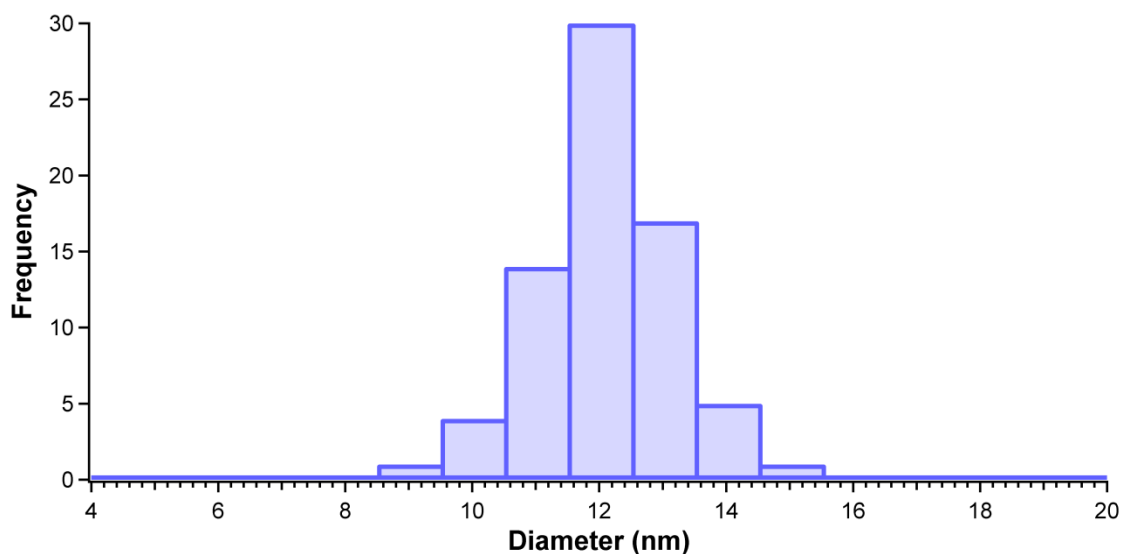


Figure 8: Size distribution of synthesized particles

Transmission electron microscopy determined slightly smaller diameters, but Haiss et al did report average deviations in the range of 11% - 18% of calculated diameters from transmission electron microscopy obtained measurements.

Concentrations were also determined by absorbance measurements once nanoparticle diameters were determined.

$$\text{Nanoparticle Concentration} = A_{450} / \epsilon_{450} l \quad (8)$$

For a path length ( $l$ ) of 1 cm the concentration is determined by the ratio of the absorbance and molar decadic extinction coefficient at 450 nm. For the calculated size of

13.45 nm, the molar decadic extinction coefficient at 450 nm was determined to be  $1.39 \times 10^8 \text{ M}^{-1} \text{ cm}^{-1}$  following the methods by Haiss et al.<sup>70</sup> The concentration was determined to be 0.86 nM, but accounting for dilution of 250  $\mu\text{L}$  of the stock solution to a total volume of 3250  $\mu\text{L}$  during measurements, the concentration of synthesized nanoparticles was determined to be 11.2 nM. However, since calculated sizes slightly differed from results obtained using transmission electron microscopy, the calculated concentrations can only be considered as approximations.

#### 4.2 Gold Nanoparticle Film

Freshly cleaned 18 x 18 mm coverslips that have undergone baths in both piranha and standard clean 1 solutions were immersed into 1 % v/v or 10 % v/v solutions of (3-aminopropyl)trimethoxysilane or (3-mercaptopropyl)trimethoxysilane for 12 - 24 hours respectively. The use of bifunctional silane molecules have been reported to form gold nanoparticle monolayers.<sup>44,45,46</sup> Functionalized coverslips were then immersed into the gold nanoparticle solution for varying amounts of time. Figure 9 demonstrates the gold particle film formation scheme.

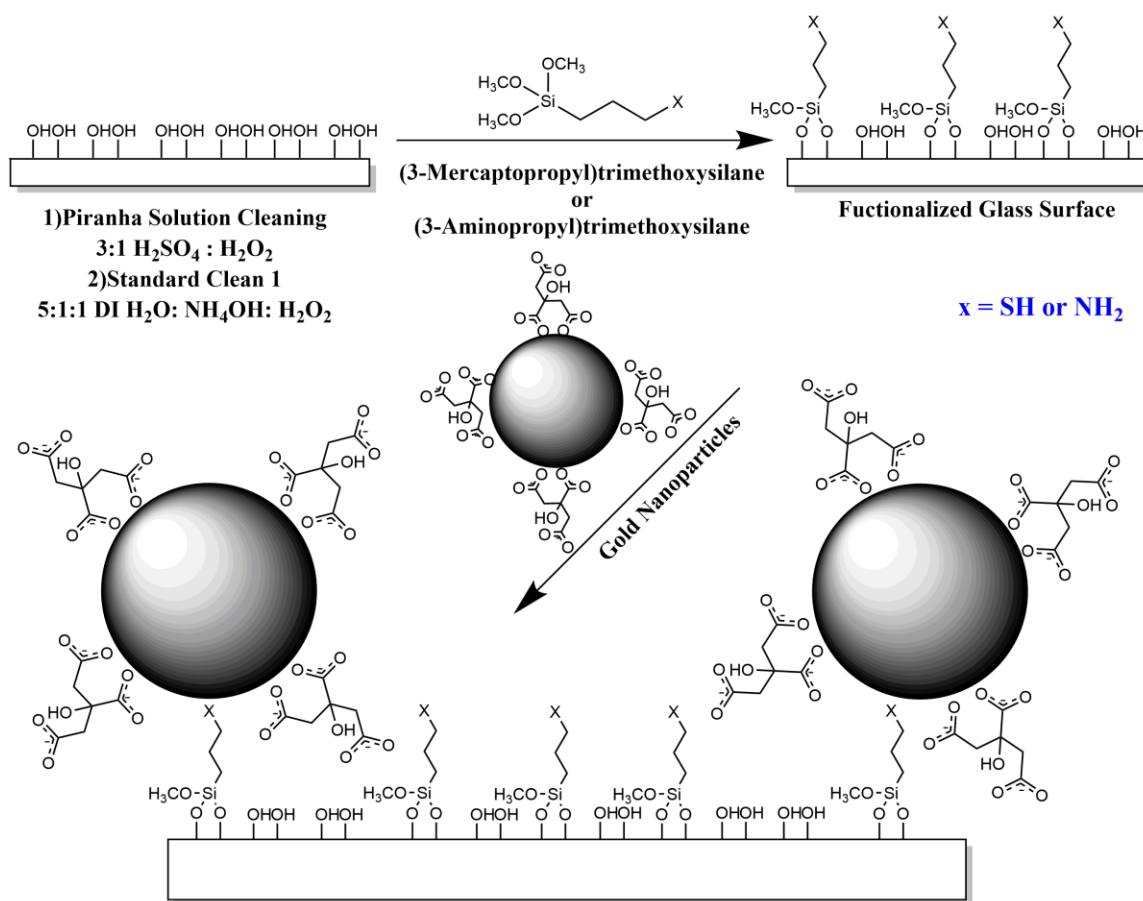


Figure 9: Gold nanoparticle film formation

Gold nanoparticle films were characterized by UV-visible spectroscopy and atomic force microscopy. Film formation is strongly dependent on concentration of the gold nanoparticle solution and immersion time.<sup>47,73</sup> The absorbance of surface-confined particles can be estimated by the surface coverage ( $\Gamma$ ) and the surface extinction coefficient ( $\epsilon_{surf}$ ).

$$A_{surf} = \frac{\Gamma \epsilon_{surf}}{6.02 \times 10^{20}} \quad (9)$$

The adsorption rate of the nanoparticles to a planar surface can further be described by equation (10).

$$\Gamma = pC\sqrt{\frac{Dt}{2}} \quad (10)$$

In equation (10),  $p$  is the probability a particle will bind to the surface,  $C$  is the solution concentration,  $t$  is time in seconds, and  $D$  is the diffusion coefficient which can further be described by equation (11).

$$D = \frac{kT}{6\pi\gamma r} \quad (11)$$

Where  $k$  is the Boltzmann constant,  $T$  is the temperature,  $\gamma$  the viscosity of the medium, and  $r$  the particle radius. It can be seen that film coverage can be controlled by immersion time as shown in Figure 10.

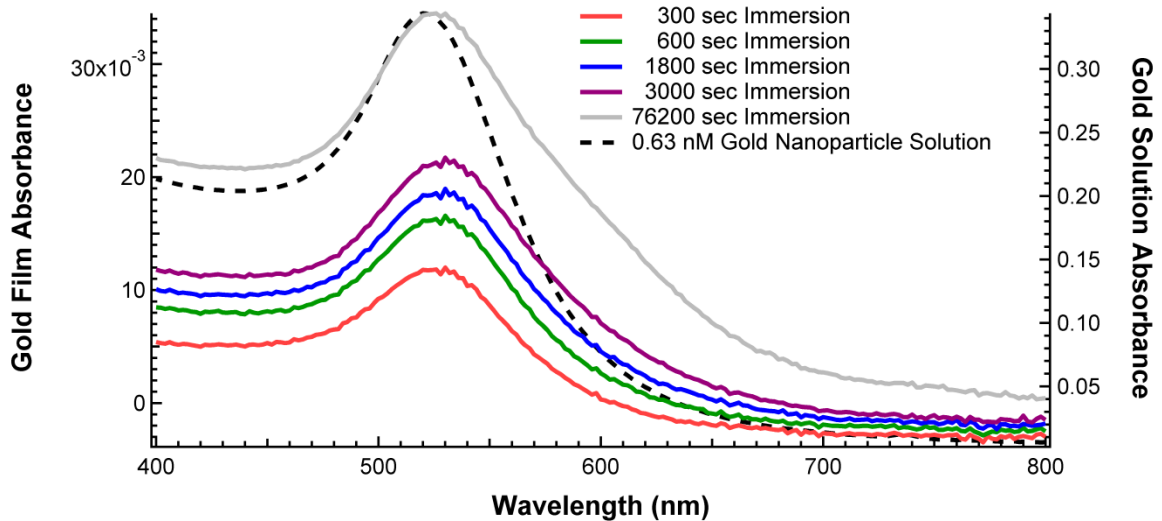


Figure 10: Mercapto functionalized film formation with increased immersion time

As shown in Figure 10, as immersion time increases absorbance at the surface plasmon resonance also increases indicating increased number of particles bound. The absorbance at the surface plasmon maximum at 525 nm versus time in seconds from the spectra in Figure 10 can be modeled by equations (9) and (10). From the model all variables could

be considered a constant  $K$  and film formation would be expected to be proportional to  $t^{(1/2)}$ .

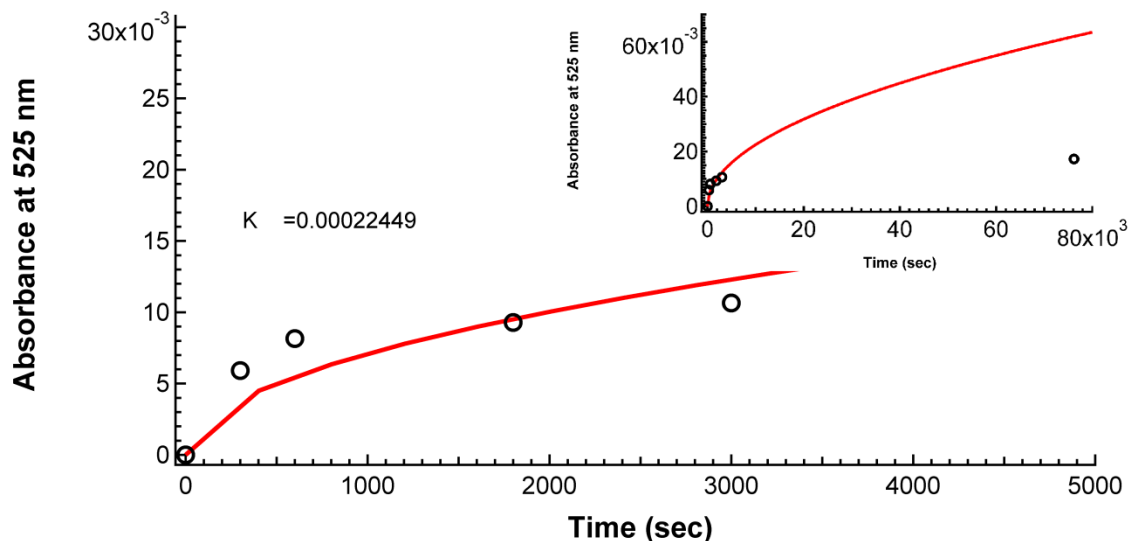


Figure 11: Absorbance at 525 nm versus time

As shown in Figure 11, at short times the model presented in equation (9) appears to be in good agreement, however, there are large deviations at longer times. The above model assumes no interparticle interactions, which is not true since particles have a negative surface charge. This surface charge is what allows the nanoparticles to be dispersed in solution, but also limits the film formation especially at longer immersion times. As the surface coverage increases the surface of the immersed coverslip obtains a stronger negative surface charge, and due to electrostatic repulsion, diffusion of particles to the binding sites become less frequent. This deviation from  $t^{1/2}$  dependence at longer times also indicates film formation reaches a saturation point. Ideal formation would be a close-packed monolayer, however, electrostatic repulsion inhibits the film formation especially when the number of remaining binding sites are low. A cubic close-packed monolayer of 12 nm Au nanoparticles would contain  $6.94E11$  particles/cm<sup>2</sup>, however, it has been

reported that only ~30 % of a close-packed monolayer can be achieved due to electrostatic repulsion at high surface coverages.<sup>47,73</sup>

Coverslips were modified with either a bifunctional silane molecule containing a mercapto or amino group as the binding site. Higher surface coverages were obtained from samples prepared with (3-aminopropyl)trimethoxysilane with one such film shown in Figure 12.

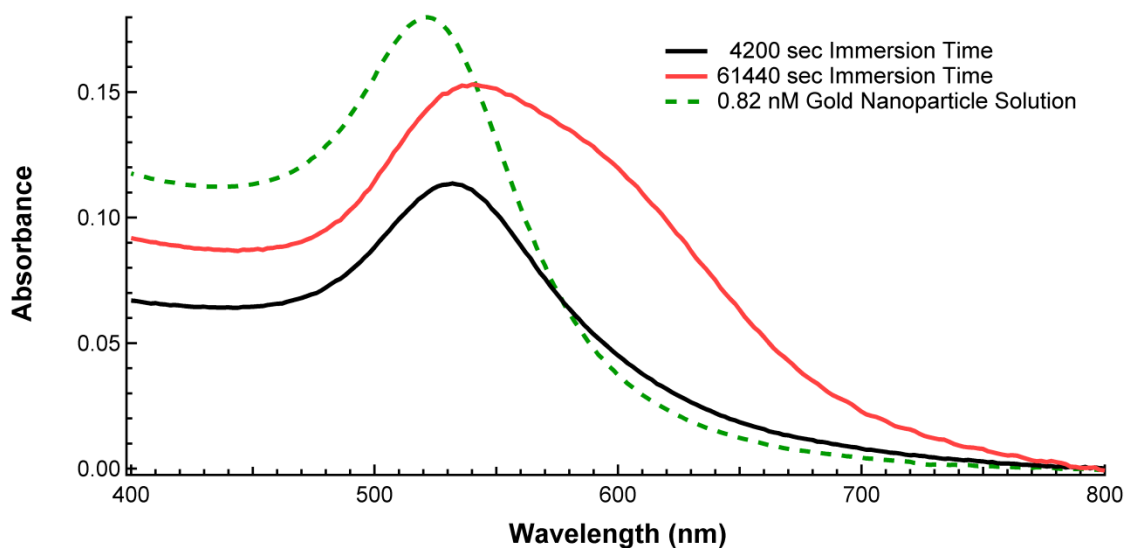


Figure 12: Amino functionalized film

Approximated surface coverages can be obtained using the surface extinction coefficient at 524 nm for 12 nm particles ( $2.8E8 \text{ M}^{-1} \text{ cm}^{-1}$ ) and the absorbance at 524 nm for the film. The approximated surface coverage for the film in Figure 12 was determined to be  $1.56E11 \text{ particles/cm}^2$ , which is approximately 22.5 % of a closed-packed monolayer a stark difference compared to the 5.3 % approximated for the film shown in Figure 10. The increase of absorbance around 600 nm is also indicative of particles being closer together due to new surface plasmon modes arising from particle-particle coupling.<sup>44,45,74</sup>

Atomic force microscopy also demonstrates high coverage in films with amino functionalization as shown in Figure 13.

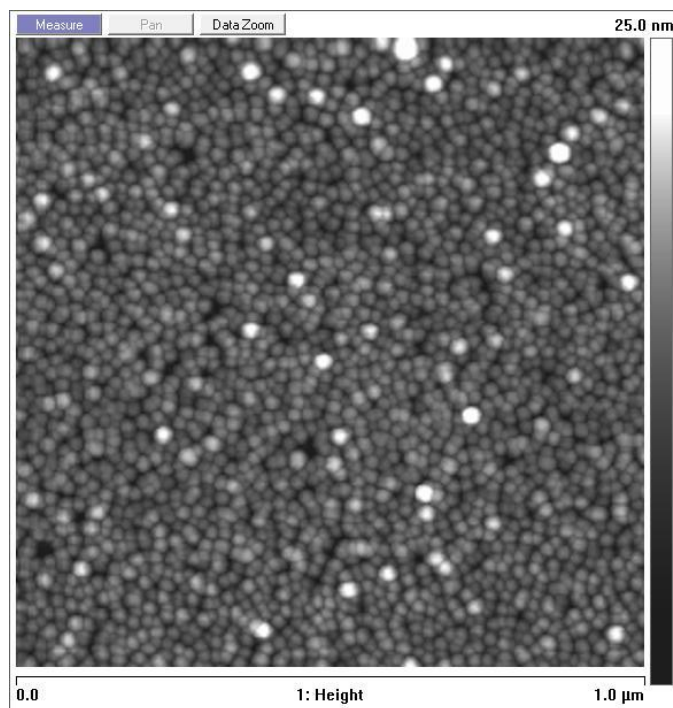


Figure 13. Amino functionalized film 1 x 1  $\mu\text{m}$  AFM image

Average surface roughness measurements were also obtained from atomic force microscopy, which yielded 2.12 nm for the film in Figure 13. These results indicate that the electrostatic attractive interaction between the amino group and negatively charged particles can overcome some of the repulsion forces seen at high coverages compared to the mercapto functionalized films, which rely on diffusion of particles close to the binding sites.

Atomic force microscopy also determined that a single layer of gold nanoparticles are formed by step height measurements. Figure 14 demonstrates a step height measurement conducted on a gold nanoparticle film that has been scratched.

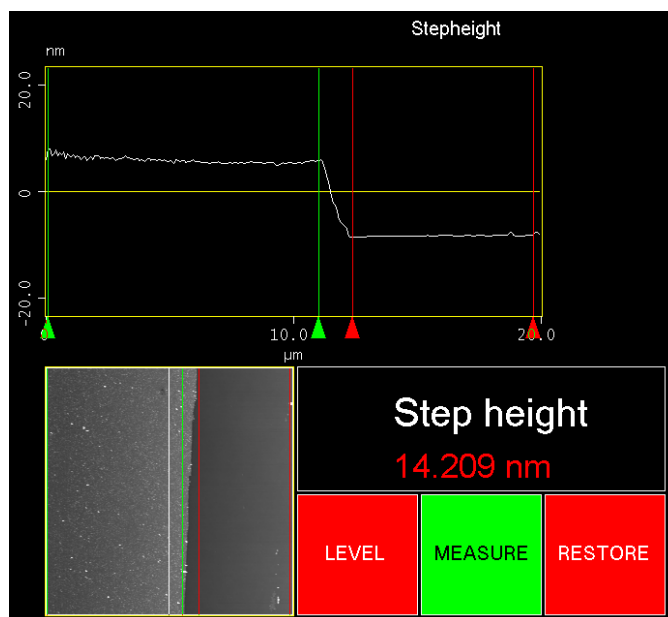


Figure 14: Step height of a gold nanoparticle film edge

As shown in Figure 14 the step height thickness of the nanoparticle film is comparable to that of the particles themselves.

#### 4.3 Polyelectrolyte Spacer Layer

Polyelectrolyte spacer layers deposited on freshly cleaned coverslips or gold nanoparticle films were characterized by atomic force microscopy. Polyelectrolyte layers were deposited with the polycation poly(allylamine) as the final layer, resulting with a spacer consisting of an odd number of layers. Figure 15 demonstrates 1 μm x 1 μm atomic force microscopy images of the largest spacer layer formed of 21 layers deposited onto a cleaned coverslip and gold nanoparticle film.

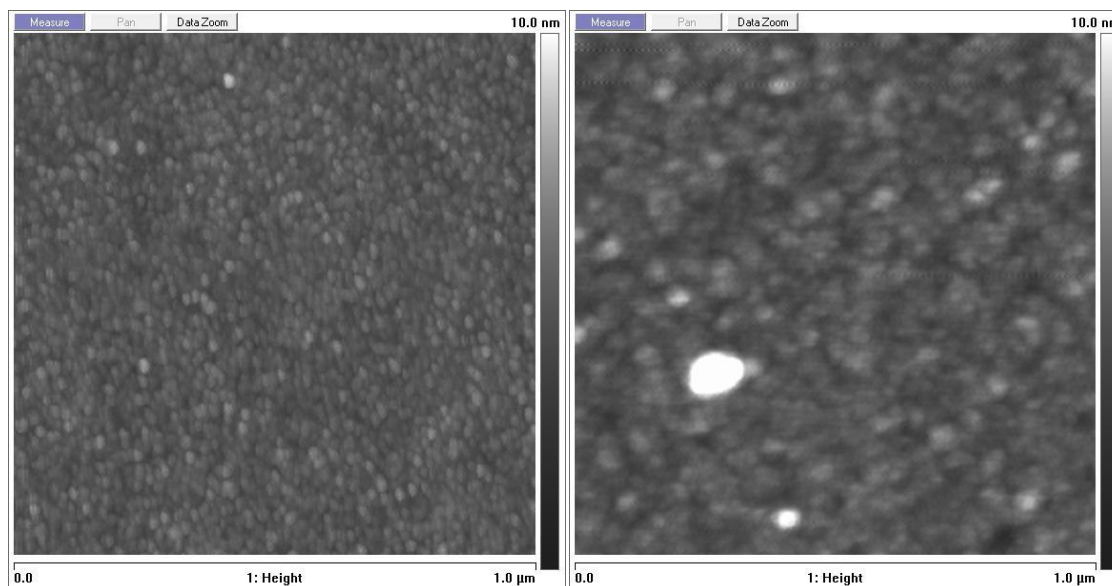


Figure 15: 21 layer spacer layer on coverslip (left) and nanoparticle film (right)

Mean surface roughness measurements also indicated there were not large deviations in the surface profile of spacer layers deposited onto coverslips with a value of 0.423 nm measured for the film in Figure 15. Similar results were seen with mean surface roughness measurements in the case of the spacer layer deposited on the gold nanoparticles films. However, mean surface roughness values measured typically were larger than those measured for spacer layers on a coverslip. With such an example demonstrated in the film shown in Figure 15, which determined a mean surface roughness of 0.650 nm. Figure 16 demonstrates the mean surface roughness for spacer layers of various thicknesses on both cleaned coverslips and gold nanoparticle films for a 1 x 1  $\mu\text{m}$  area.

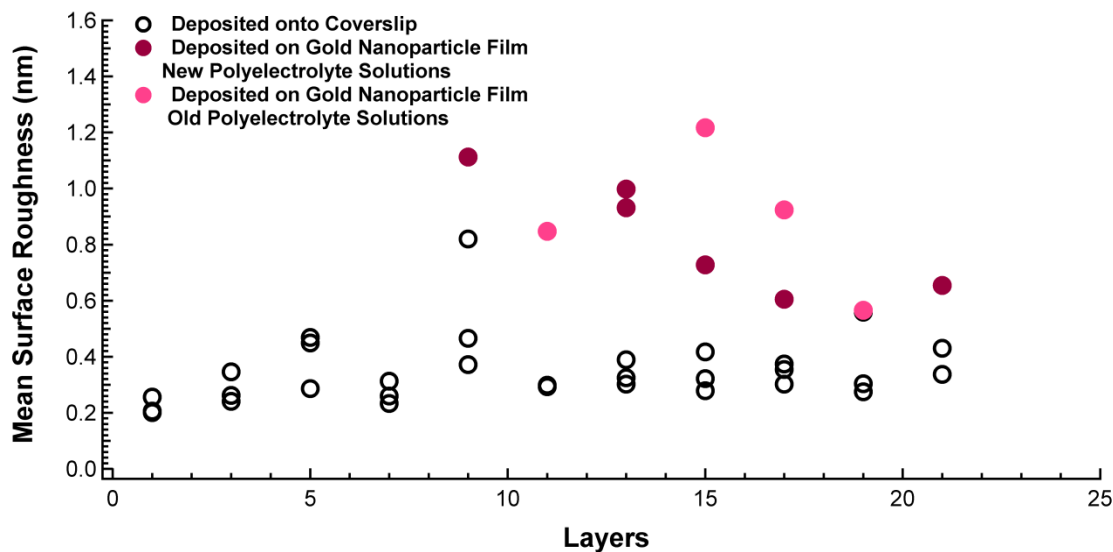


Figure 16: Mean surface roughness versus number of layers

As shown in Figure 16 the mean surface roughness for polyelectrolytes deposited onto coverslips appears to be within a constant range (0.2-0.4 nm) regardless of the number of layers deposited. Larger values typically were measured for spacer layers on gold nanoparticle films. As seen in Figure 16 the two sets of points for polyelectrolyte layers deposited on gold are labeled whether new pristine polyelectrolyte solutions were used prior to deposition or whether the polyelectrolyte solutions were at least several days old, as the age of the polyelectrolyte solutions appeared to affect spacer layer formation as will be discussed later. However, regardless of the age of the polyelectrolyte solution the mean surface roughness tends to decrease with number of layers deposited due to the "smoothing" of the surface with more layers deposited as a more complete coverage is obtained.<sup>68</sup>

The thickness per number of layers deposited was also measured for polyelectrolytes layers on cleaned coverslips and approximated for layers deposited onto

gold nanoparticle films. Films were scratched to form step-edges to determine step heights as shown in Figure 17.

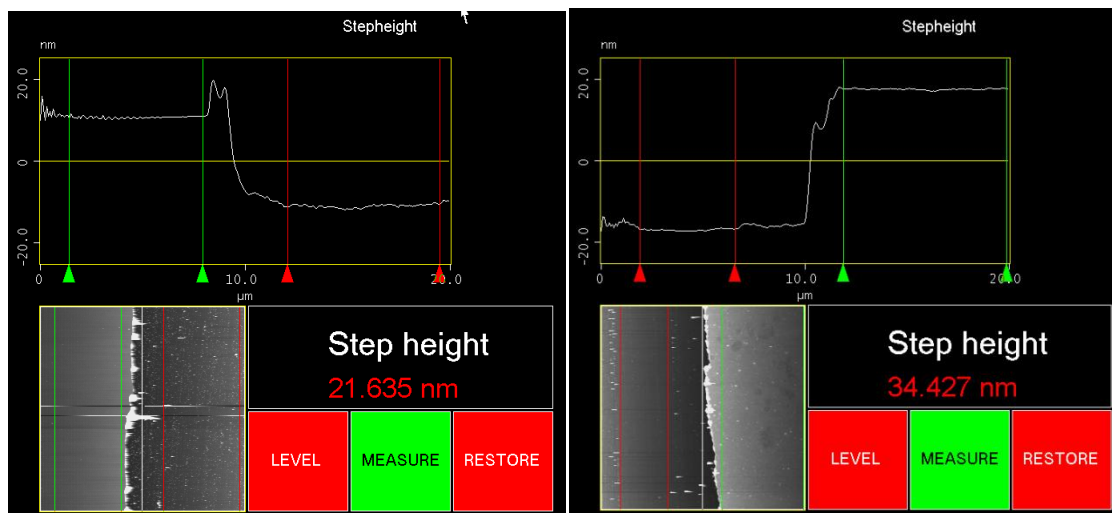


Figure 17: 21 layer spacer on coverslip (left) and nanoparticle film (Right)

In Figure 17 the difference in step height is comparable to the size of the nanoparticles. UV-vis absorbance measurements also demonstrated how the surface plasmon resonance of the nanoparticle film was affected from the deposition of the polyelectrolyte layers as shown Figure 18.

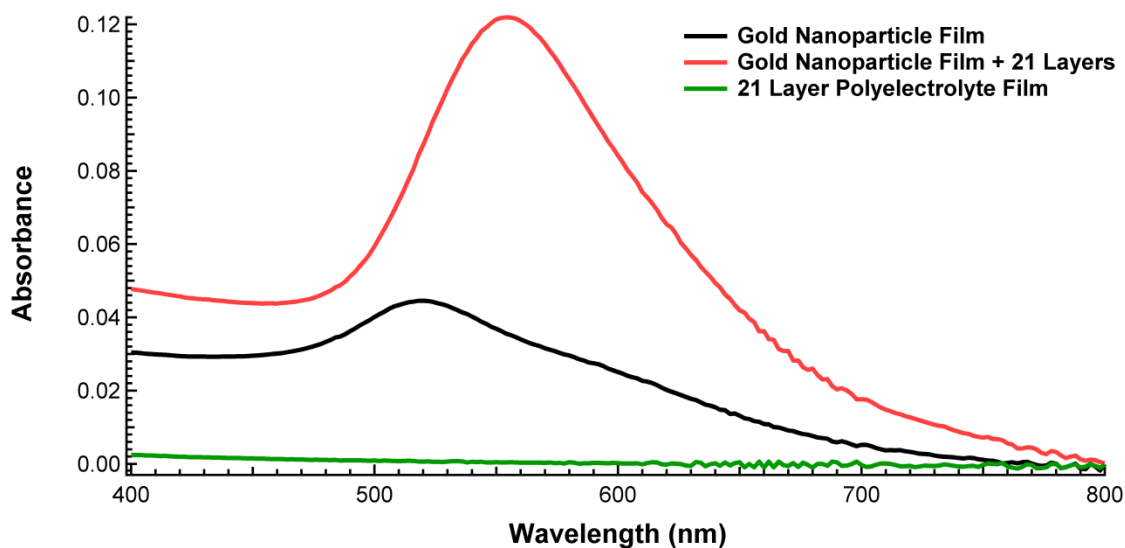


Figure 18: UV-Vis absorbance of nanoparticle film before and after spacer deposition

As shown in Figure 18 an increase in intensity and as well as a red shift of the surface plasmon resonance was accompanied with the deposition of the polyelectrolyte spacer layer. Also seen in Figure 18 is the absorbance spectrum for a 21 layer polyelectrolyte film on a coverslip which shows no distinct absorption bands, indicating the changes seen on the nanoparticle film are from a change in the local dielectric constant of the surrounding medium of the nanoparticles.<sup>68</sup>

Thicknesses of spacer layers on gold nanoparticle films were approximated by subtraction of the average step height of gold nanoparticle films, which was determined to be  $13.380 \pm 1.195$  nm. Figure 19 demonstrates these thicknesses as a function of number of layers along with thicknesses for polyelectrolyte films deposited onto coverslips.

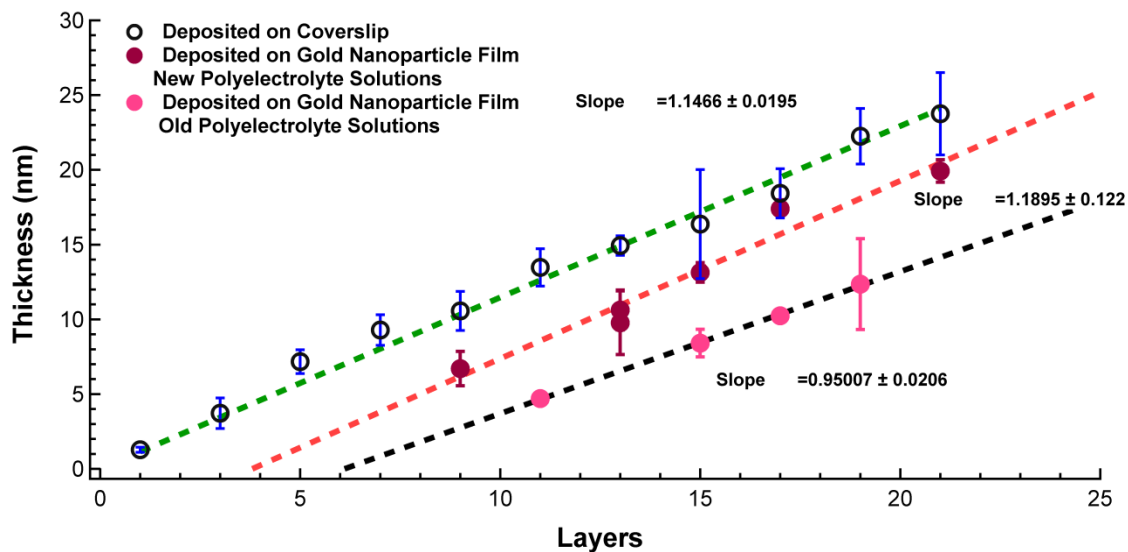


Figure 19: Thickness versus number of layers on coverslip and nanoparticle films

As shown in Figure 19 the spacer layer thickness versus number of layers deposited follows a linear trend. On a coverslip the thickness of the spacer layer is approximately increased by 1.15 nm per layer. Spacer layers deposited on gold nanoparticles using new pristine polyelectrolyte solutions also appeared to follow the same trend with approximately 1.19 nm deposited per layer, however, the overall thickness of the spacer layer was determined to be thinner than a spacer layer of the same number of layers deposited onto coverslips. This can be attributed to the filling in of space between particles for the first few layers deposited.<sup>68</sup> Spacer layers deposited using old polyelectrolyte solutions also followed a linear trend, however, deviates from the trends for spacer layers deposited using new polyelectrolyte solutions on both coverslips and nanoparticle films. The thickness of these layers were thinner than layers on coverslips as well as the layers on particles deposited using new solutions. The thickness per layer was also smaller with an approximate value of 0.95 nm per layer. Upon inspection of atomic

force microscopy images it can be seen that large deviations occur on several areas of the films as shown in Figure 20.

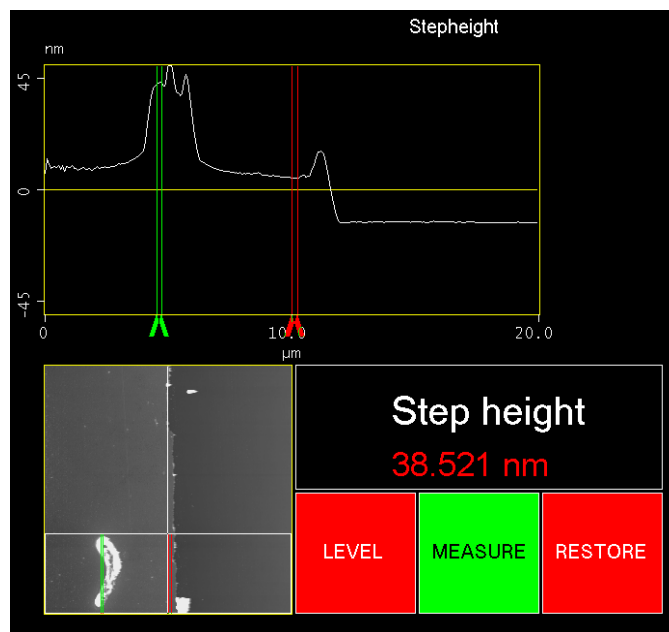


Figure 20: 11 layers on gold nanoparticle film using old polyelectrolyte solution

This area in Figure 20 appeared to be approximately 38 nm taller than the rest of the area, which was approximately 4.6 nm thick on top of nanoparticles. These thicker regions were only present when old polyelectrolyte solutions were used during deposition and are suspected to be aggregates of polyelectrolytes that bind during deposition. These areas were ignored during the spacer layer thickness approximations. However, these areas suggest that once aggregates begin to form within the solutions the concentration of the polyelectrolytes dissolved within the solution is now less resulting in thinner spacer layers being deposited and resulting thicker regions similar to that shown in Figure 20.

#### 4.4 Single Molecule Spectroscopy

Quantum dot samples were obtained from Dr. Andrew B. Greytak's group at the University of South Carolina. Particle solutions consisted of a 4 nm CdSe core

surrounded by a 1 nm CdS shell, which displayed an exciton absorbance and emission maximum at 600 nm and 610 nm respectively as shown in Figure 21.

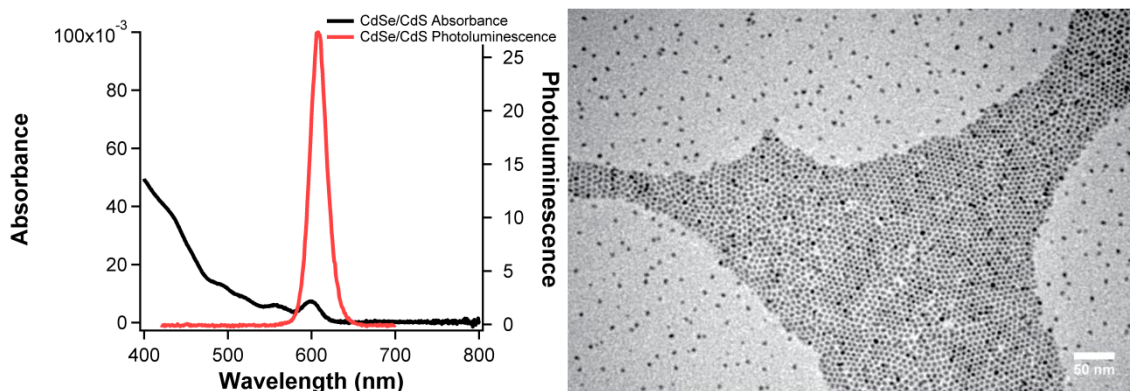


Figure 21: UV-Vis/PL spectrum and TEM image of CdSe/CdS quantum dots

Figure 21 also demonstrates a transmission electron microscopy image of the 6 nm particles (50 nm scale bar), which was provided by Dr. Greytak's group.

As mentioned earlier, in order to compete with the Auger recombination process the multiexciton emission rate must be enhanced, which is strongly correlated to the spectral overlap between the multiexciton state and the surface plasmon resonance. However, the multiexciton state is difficult to measure due to the same Auger recombination, but has been reported to having a similar energy as the single exciton state.<sup>12</sup> Figure 19 displays the spectral overlap between gold nanoparticle films with various spacer thicknesses and the absorbance as well as emission spectra of the CdSe/CdS quantum dots used in single molecule experiments.

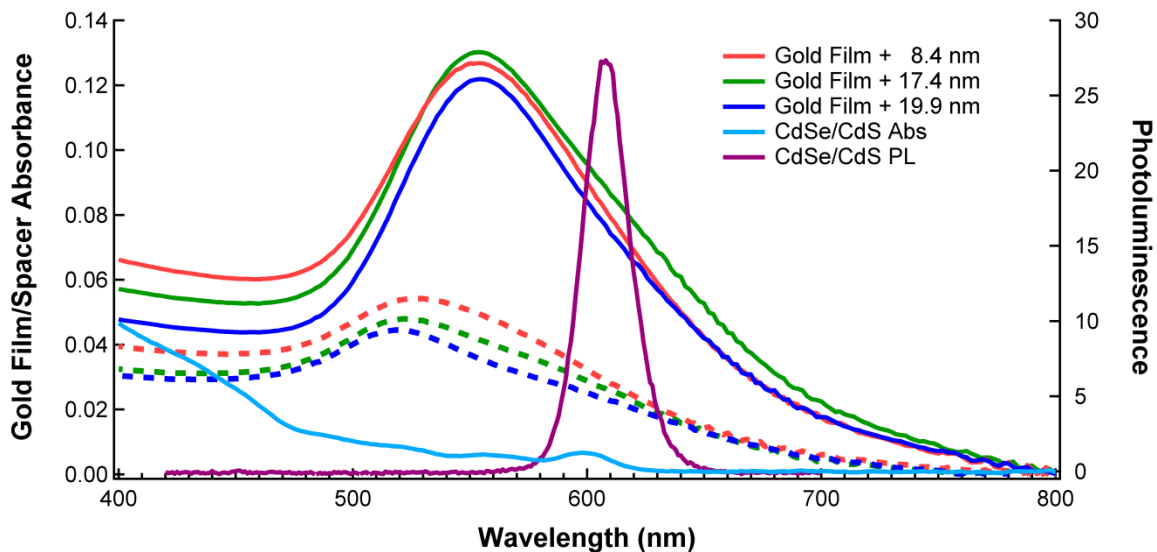


Figure 22: Spectral overlap of films and quantum dots

As seen in Figure 22 there isn't complete overlap between the surface plasmon resonance maximum of the nanoparticle/spacer films and the quantum dots, but there have been reports of enhanced emission rates occurring off the resonance maximum as the maximum overlap is expected to just have the largest effects.<sup>23,43</sup>

As mentioned earlier multiexcitons can be created in two ways; absorption of a photon with an energy at least several times the bandgap energy or by sequential absorption of two or more photons with an energy at least that of the bandgap energy. Excitation was done with a 470 nm ( $\sim 2.6$  eV) pulsed diode laser, which cannot create a multiexciton with a single photon within the  $\sim 2.0$  eV bandgap CdSe/CdS nanoparticles. Using estimated absorption cross sections the average number of absorbed photons per excitation pulse can be calculated. An extinction coefficient ( $\epsilon$ ) of  $3.97 \times 10^6 \text{ M}^{-1} \text{ cm}^{-1}$  was determined by Dr. Greytak's group at 350 nm for the CdSe/CdS nanoparticles. Equation (12) demonstrates how the extinction coefficient is directly related to the absorption cross section.<sup>75</sup>

$$\sigma = 3.82 \times 10^{-21} (\epsilon) \text{ (in cm}^2\text{)} \quad (12)$$

Equation (12) yields an absorption cross section of  $1.52\text{E-}14 \text{ cm}^2$  at 350 nm. However, excitation in this work was conducted at 470 nm. To estimate the absorption cross section at 470 nm the ratio of the absorbance at 470 nm to 350 nm was taken into account and used to determine an absorption cross section ( $C_{\text{abs}}$ ) of  $4.50\text{E-}15 \text{ cm}^2$  at 470 nm. To calculate the average number of photons absorbed per pulse ( $\langle N \rangle$ ) the following equation was used.<sup>76</sup>

$$\langle N \rangle = \frac{C_{\text{abs}} \times \text{power}}{\text{photon energy} \times \text{spot area} \times \text{laser repetition rate}} \quad (13)$$

The spot diameter was assumed to be diffraction limited (14).

$$\text{Spot diameter} = \frac{1.22 \times \lambda \text{ (cm)}}{NA} \quad (14)$$

Where  $\lambda$  is the excitation wavelength in centimeters, and NA the numerical aperture of the objective. For a 470 nm ( $4.70\text{E-}5 \text{ cm}$ ) excitation and an objective with a numerical aperture of 1.25 the diffraction limited spot diameter was determined to be  $4.59\text{E-}5 \text{ cm}$ , and would indicate the spot area to be  $1.65\text{E-}9 \text{ cm}^2$ . For a photon energy of  $4.22\text{E-}19 \text{ J}$  at 470 nm excitation, 10 MHz repetition rate, and  $1.22 \mu\text{W}$  power used for experiments the  $\langle N \rangle$  was determined to be 0.78. Assuming Poisson statistics the probability that more than one photon is absorbed at this power is 0.19.

Quantum dots on a clean coverslip were used as the control for these experiments.

Figure 20 demonstrates the imaging capabilities of the laser scanning confocal microscope.



Figure 23: 75 x75  $\mu\text{m}$  (left) and 1.15 x 1.15  $\mu\text{m}$  (right) images of CdSe/CdS particles

Figure 23 shows a 1.15 x 1.15  $\mu\text{m}$  image of a single CdSe/CdS nanoparticle, but the confocal setup can scan and collect photons from a single pixel. On this single pixel excited state fluorescence decays, blinking traces, and photon correlation can be obtained.

The confocal system however, cannot collect all three simultaneously.

#### 4.4.1 Plasmon-Exciton Coupling

Excited state fluorescence decays can be obtained to monitor the excited state dynamics of individual particles. Figure 24 demonstrates an excited state decay of a single CdSe/CdS nanoparticle with an average lifetime of 22.405 ns.

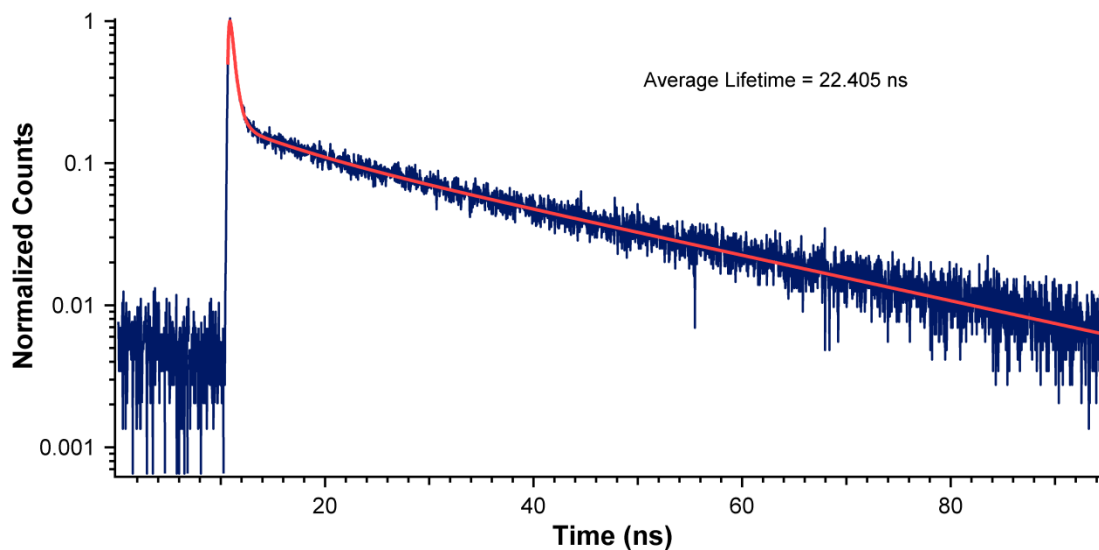


Figure 24: Single quantum dot excited state fluorescence decay

As seen in Figure 24 quantum dot excited state decays are not single exponential indicating several processes are responsible in the decay of the excited state. The decay in Figure 24 along with all the quantum dots analyzed needed three or four time constants to give adequate fits. The decay counts can be totaled and the sum can be treated as a relative quantum yield since the collection time on each particle was the same and plotted versus the average lifetime of that particle as shown in Figure 25.

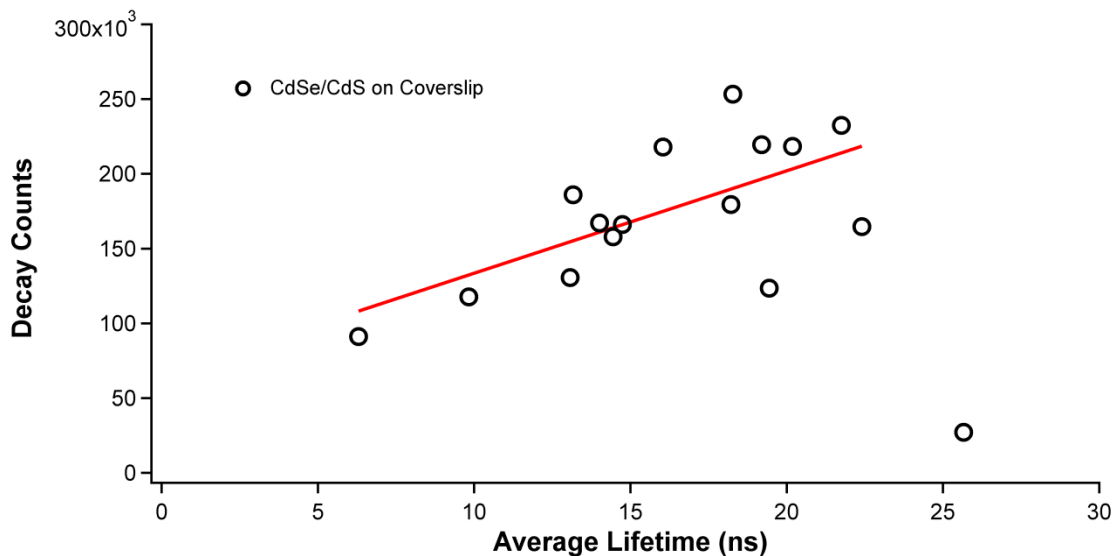


Figure 25: Decay counts versus average lifetime of CdSe/CdS particles

The increase in average lifetimes with total counts demonstrate that the non-radiative processes are dominant in the changes measured in the decay of the excited state. This also suggest that in cases of high counts and long lifetimes the main decay process is nearing that of just radiative recombination, which has a longer lifetime than what is normally measured as the average lifetime.

In the case of probing enhancement of the emission rate this suggest that the reported decrease in average lifetimes known to occur is not adequate alone to determine whether enhancement of the radiative rate is occurring. However, blinking dynamics have been reported to aid in determining the emission rate of single particles. Blinking traces can be collected simultaneously with excited state decays. Figure 26 shows the corresponding blinking trace to the excited state decay in Figure 24.

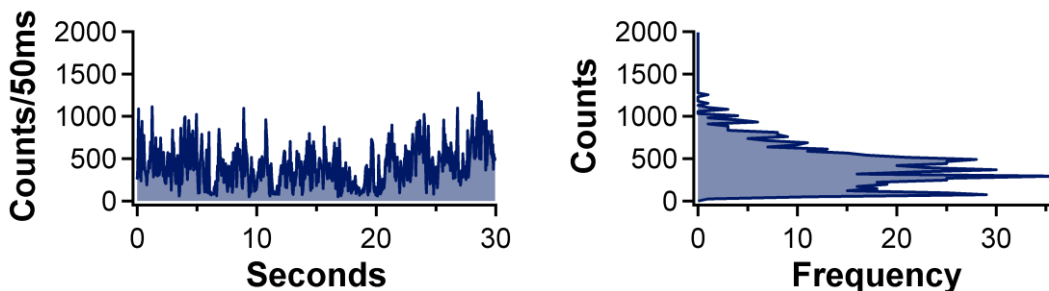


Figure 26: Single particle blinking trace (left) and histogram of counts per bin (right)

Blinking traces give insight into the decay dynamics of the excited state. Where periods of low emitting counts can be attributed to the particle being in an off state. Likewise, periods of high emitting counts can be considered for the particle to be in an on state. However, as seen in Figure 26 the fluctuation in emitting counts also demonstrate that various non-radiative decay channels are dominant for changes in the recombination process. It has been proposed that the periods of the highest emitted counts would resemble the particle in its brightest state. Fisher et al. proposed that the decay dynamics in these brightest moments would resemble the excited state decaying just purely by radiative recombination, therefore the emission rate could be measured.<sup>77</sup> Excited state decays of the quantum dot in these brightest moments can be constructed using the methods used by Wu et al.<sup>78</sup> One decay was formed from photons in bins where the counts exceeded 70% of the max. Another was formed from photons in bins below 10% of the max as shown in Figure 27.

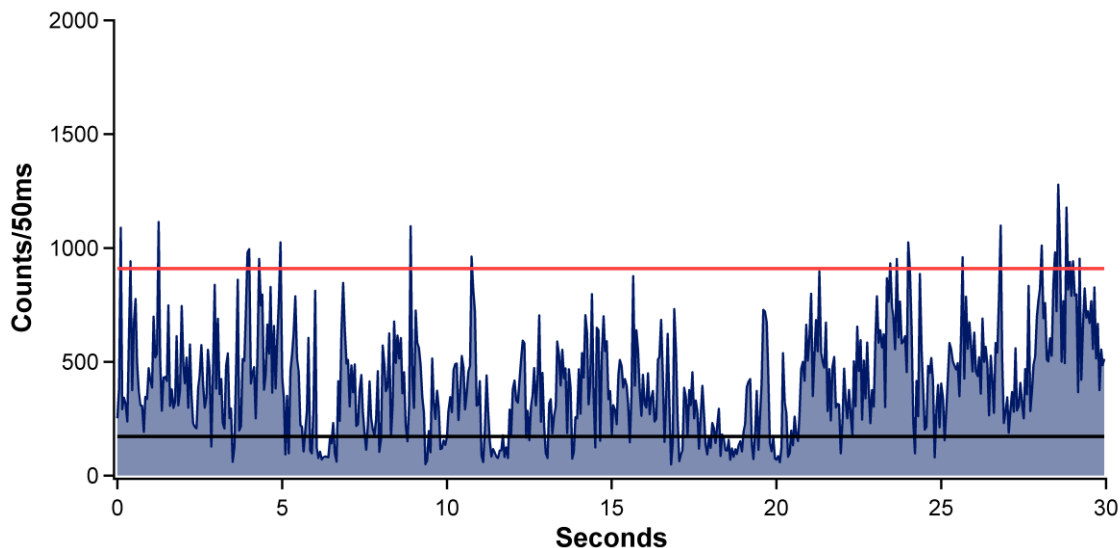


Figure 27: 70% threshold (red) and 10% threshold (black)

The photons used to form the above 70% excited state decay would include the photons emitted when the particle is its brightest state, but would also include background counts from the surrounding matrix. To eliminate these background counts a decay is formed from photons below the 10% threshold, where as seen in Figure 25 (below black line) the particle is in an off or low emitting state. Photons in this case would mostly consist of any photons arising from the surrounding matrix. The below 10% decay was normalized by the ratio of the total time the particle spent emitting above the 70% threshold to the total time the particle spent emitting below the 10% threshold and subtracted from the decay formed from the particle being in the brightest state. This maximum intensity corrected decays, which will be referred to as emission rate decays, needed one or two time constants to give adequate fits as shown in Figure 28.

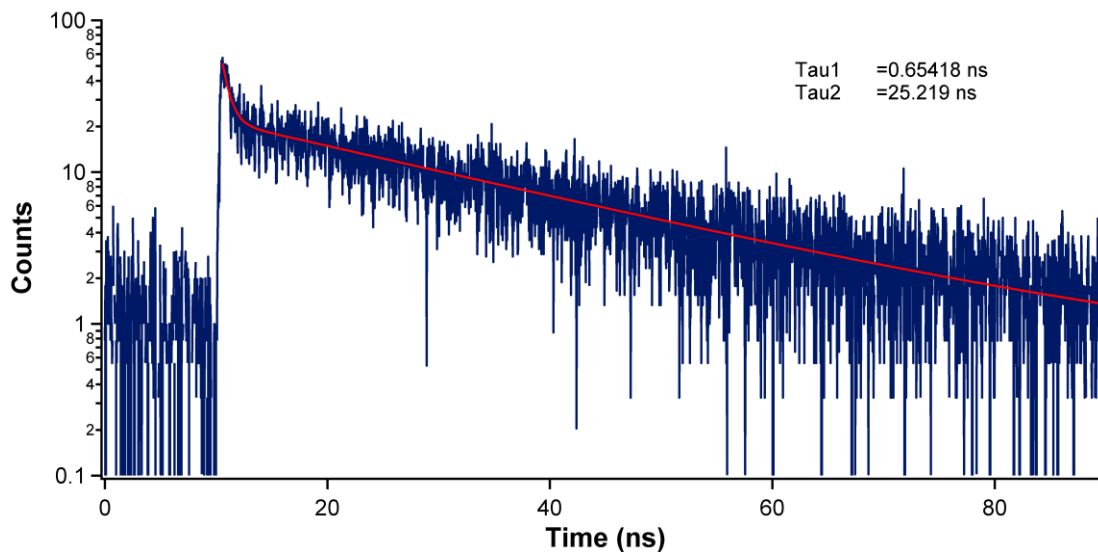


Figure 28: Emission rate decay formed from blinking trace in Figure 27

In Figure 28 two time constants were needed to give an adequate fit. The fast component seen with a time constant of 0.65418 ns could arise from the background being not completely removed or biexciton emission, however, uncertainty in its origin led to it not being included in the analysis and would need further investigation. The second time constant of 25.219 is in agreement with reported values of emission lifetimes determined for CdSe quantum dots.<sup>77</sup> Furthermore, small deviations from this value were measured for all the particles measured on coverslips as seen in Figure 29.

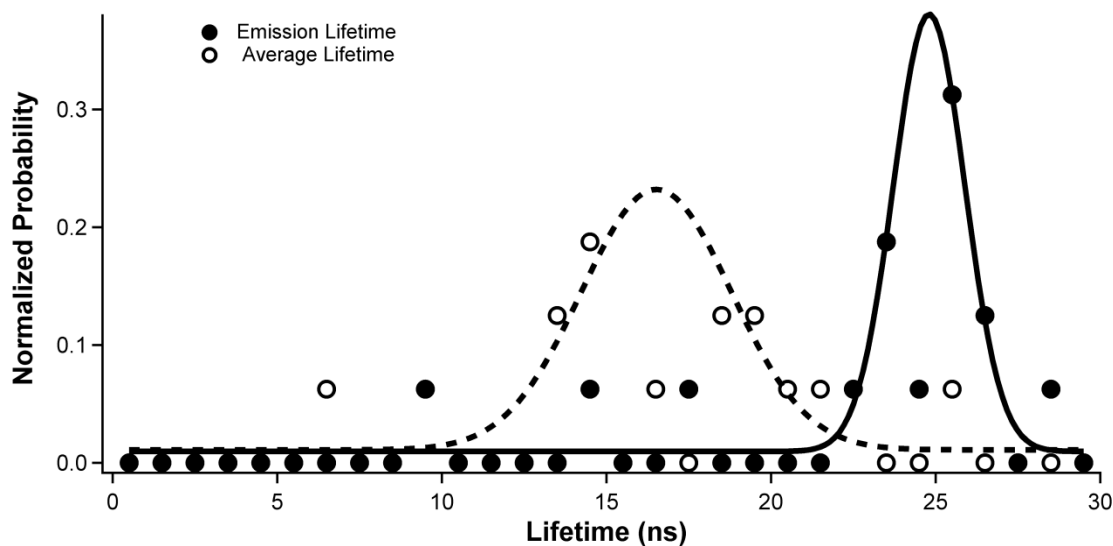


Figure 29: Emission and average lifetimes of CdSe/CdS quantum dots

As seen in Figure 29 there is a small deviation in the emission lifetime for a majority of the quantum dots, as would be expected for nanoparticles within the same sample. There are larger deviations in the average lifetimes measured, which had shorter lifetimes than those measured for the emission process. Again indicating how the non-radiative processes greatly affects the average lifetime measured from particle to particle within the same sample.

The emission rate was then determined for 50 CdSe/CdS quantum dots measured at each distance from gold nanoparticles. Figure 30 shows how the emission lifetime changes with distance from gold nanoparticles.

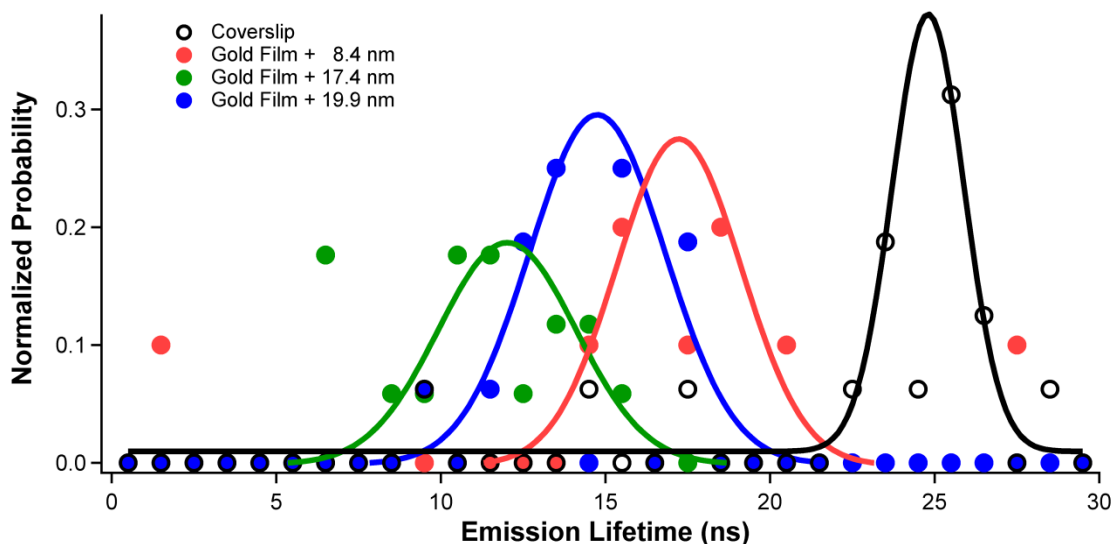


Figure 30: Modified emission lifetimes in the presence of gold nanoparticles

In the presence of gold nanoparticles it is clearly seen that the emission rates become faster (shorter lifetimes). The distance-dependence is also seen as the emission lifetime distributions shift depending on distance from the gold particles. At a spacer distance of 8.4 nm the emission lifetimes are shortened, and become even shorter at approximately twice the distance at 17.4 nm. At the even further distance of 19.9 nm the emission lifetimes appears to lengthen again, but are relatively shorter than the emission lifetimes at a distance of 8.4 nm. Multiple processes are known to be introduced in the presence of gold nanoparticles. Enhancement of the emission rate can occur as well as non-radiative energy transfer, so the shortening of the emission lifetime cannot determine that pure emission enhancement is occurring as energy transfer is a competing process, which is also distance-dependant. To further probe the interaction at the specific distance the relative quantum yields were determined in a similar manner to Figure 25 for the emission rate decays of the quantum dots on a coverslip and in the presence of gold nanoparticles.

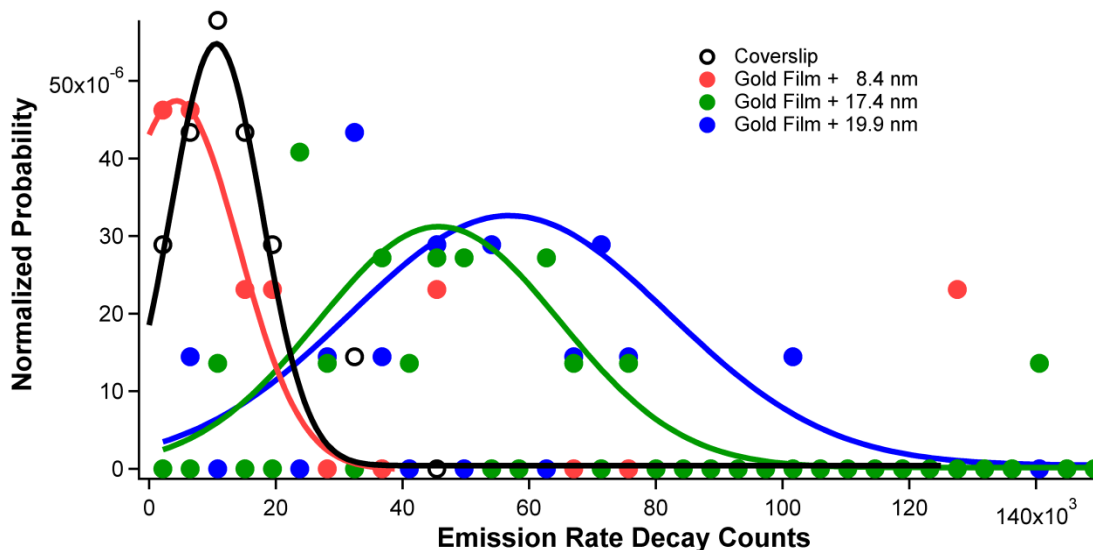


Figure 31: Modified emission counts in the presence of gold nanoparticles

It is clearly seen the total number of counts change in the emission rate decays in the presence of gold. Figure 31 and Figure 30 together could approximate relative contributions of the competing processes at the specified distance. At a spacer distance of 8.4 nm the emission lifetime shortens slightly, but the total amount of counts are slightly less than the control of quantum dots on just a coverslip. It could be estimated that since the emission rate increases (shortened emission lifetime) emission enhancement ( $\Gamma_m$ ) is occurring due to plasmon-exciton coupling, but slightly less overall counts indicate energy transfer ( $K_{et}$ ) is occurring as well. Since the decrease in overall counts is slightly less it could be estimated that in this case the relative contributions are approximately  $\Gamma_m \sim K_{et}$ .

At the spacer distance of 17.4 nm the shortest emission lifetime was measured (fastest emission rate), as well an approximate 4-fold increase in the emission counts. Indicated from the shortest emission lifetime measured the plasmon-exciton coupling is stronger than in the case of the 8.4 nm spacer distance, which is also supported by the

large increase in counts. In this case it could be estimated that  $\Gamma_m \gg K_{et}$ . At the spacer distance of 19.9 nm the emission lifetime actually increased relative to the emission lifetime measure at a distance of 17.4 nm, which would indicate a slightly weaker plasmon-exciton coupling. However, an approximate 6-fold increase in counts was measured. This could be explained by less energy transfer at the farther distance, which could compensate for the less efficient plasmon-exciton coupling at this distance.

Blinking dynamics were also modified in the presence of gold nanoparticles as shown in Figure 32.

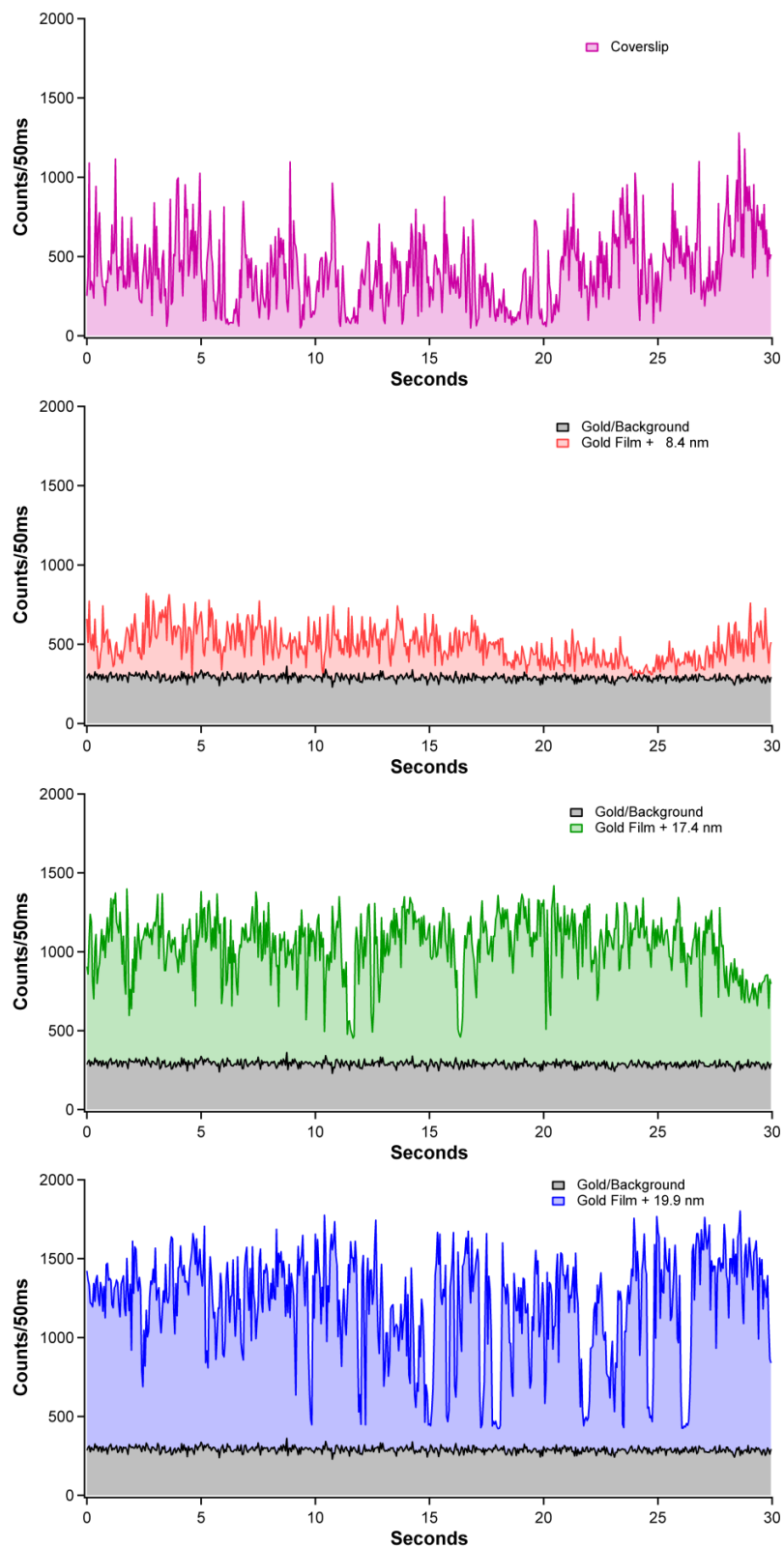


Figure 32: Blinking dynamics of four quantum dots

It is clearly seen in Figure 32 that the blinking dynamics change in the presence of Gold nanoparticles. As seen for the quantum dot on a coverslip the intensity varies and periods in which the particle has reached an off state (minimum counts) occur frequently. However, in the presence of gold particles the intensity deviates less and increases. At the distance of 8.4 nm the intensity does not deviate greatly (~500 counts), but the overall counts are less than the quantum on a coverslip. Which would be expected if a slight plasmon-exciton interaction is occurring as well as energy transfer. At the distance of 17.4 nm the increased intensity does not deviate greatly and less minimums in the blinking trace occur (suppressed blinking). Suppressed blinking is thought to occur because the emission rate has been enhanced to the point where ionization events have become less probable because radiative recombination is the favorable process. At this distance gray states are also seen. For comparison the counts due to gold/background have been shown. If a quantum dot has gone into an off (low or non-emitting) state it would be expected that the off state would have the same intensity as the gold/background. However, this is not the case. The low emitting periods of the quantum dot 17.4 nm away from gold particles demonstrate higher counts than what would be expected for just gold/background, and indicates that the emission rate of charged quantum dots are being enhanced in the presence of gold nanoparticles as well.<sup>23</sup> At the farthest distance of 19.9 nm the intensity increases (~1500 counts) even more, but minimums in the blinking trace occur more frequently. Which is what would be expected in the case of less efficient plasmon-exciton coupling, but less energy transfer at this distance results in overall higher intensities.

The percentage of time that a quantum dot spends in an on (emissive) state can be approximated by applying a 10% threshold, which would designate bins with photon counts higher than the threshold as on. This on state percentage is an attempt to apply a value to the degree of suppressed blinking that occurs in the presence of gold.

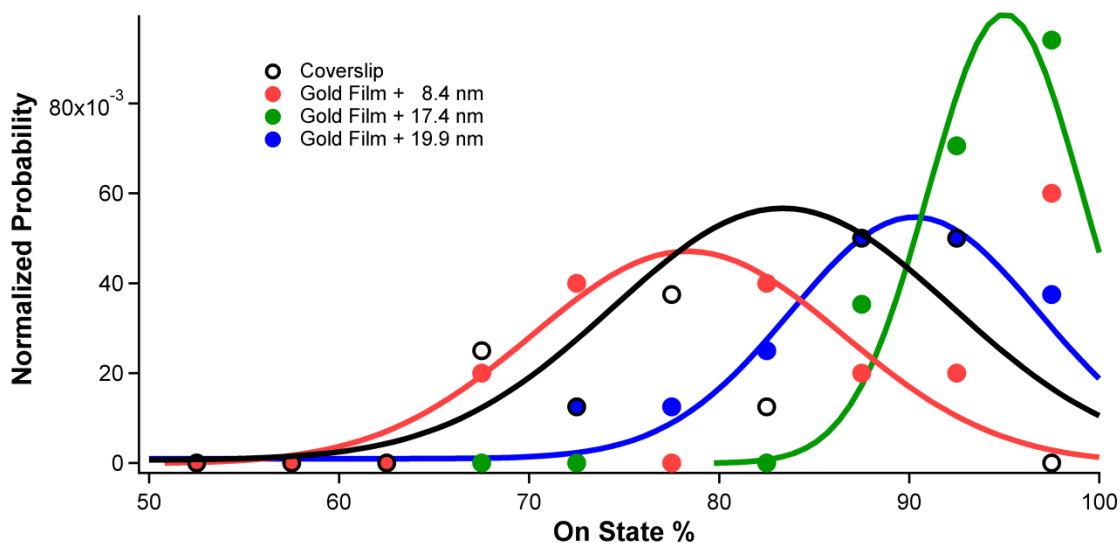


Figure 33: On state percentage in the presence of gold nanoparticles

On a coverslip the quantum dots have a large distribution of total time spent in an on state as seen in Figure 33, which is expected due to differences in the non-radiative processes from particle to particle. At the 8.4 nm distance from Gold particles the distribution shifts to a slightly less time being in an on state. This could be explained from the approximated equal contributions of enhanced radiative rate and energy transfer. Energy transfer is an additional non-radiative process introduced by the gold particles and could explain the slight shift to less on state percentage. At approximately twice the distance at 17.4 nm the on state percentages become quite high, which is an agreement with the highest emission rates measured in these experiments. At the farthest distance of 19.9 nm the on state percentages are considerable high, but are less than the on state percentages

measure at 17.4 nm. Which is also in agreement with an approximated weaker plasmon-exciton interaction relative to the interaction at 17.4 nm.

#### 4.4.2 Plasmon-Multiexciton Coupling

The Hanbury Brown-Twiss geometry can determine whether photons are correlated.<sup>72</sup> In this geometry the stop associated with time correlated single photon counting is no longer the laser excitation pulses. Signal is split between two detectors where one is designated as the start and the other the stop, and the measured time delays are correlated into a histogram. Collection in this manner can determine whether multiple photons are emitted with the rise of a peak centered about a time delay of zero. Since two detectors are used where one is designated as the start and the other as the stop, a time delay of zero would indicate simultaneous detection of a photon at each detector.

Antibunching behavior is said to be displayed when there is no peak at the time delay of zero. Quantum dots are known to display antibunching behavior since emission from multiexciton states is an inefficient process since Auger recombination is the dominating process. Most of the CdSe/CdS quantum dots on a coverslip displayed antibunching behavior where there is little or no peak at the time delay of zero.

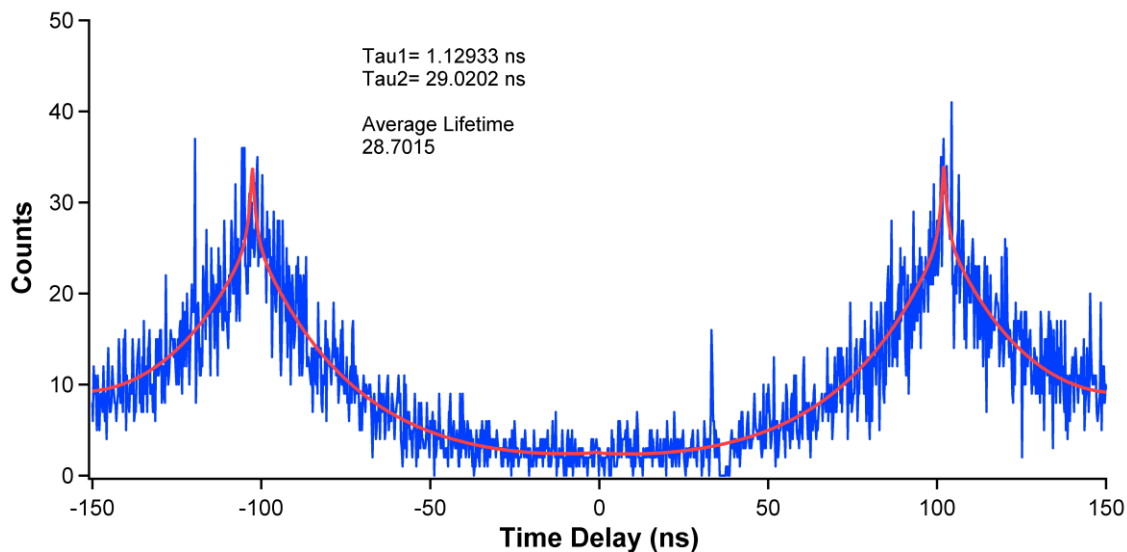


Figure 34: Photon correlation histogram of CdSe/CdS quantum dot on coverslip

Figure 34 shows lack of a peak at a time delay of zero, indicating this quantum dot was displaying antibunching behavior. As seen in Figure 34 two side peaks arise at a time delay of  $\pm 100$  ns. The excitation repetition rate used was 10 MHz, which indicates there is a 100 ns period between pulses. These side peaks can then be seen as the excited state decay normally collected in time correlated single photon counting experiments, which happens to be symmetrical about the  $\pm 100$  ns time delay. Double sided exponential functions of two or three time constants were needed to determine average lifetimes of these peaks.

Photon correlation histograms of quantum dots in the presence of gold nanoparticles contained significant background counts as shown in Figure 35.

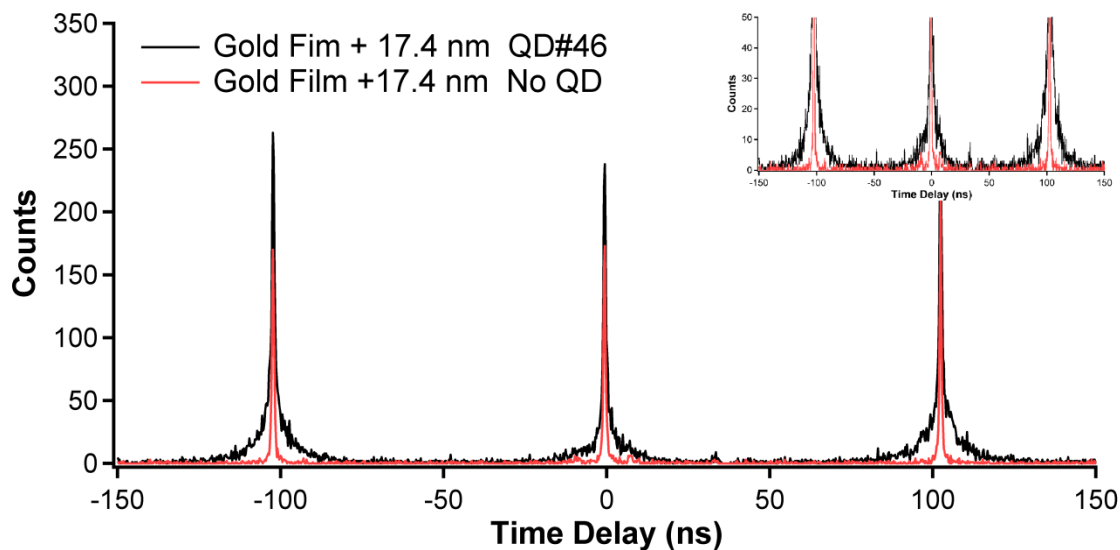


Figure 35: Photon correlation histogram of quantum dot in the presence of gold

As seen in Figure 35 the sharp features that arise in the peaks can be attributed to counts from the background which is indicated by the photon correlation histogram of an area with no quantum dot present. This background signal could be scatter or fluorescence from the gold nanoparticles, which have been reported to have fast fluorescence lifetimes due to fast decay of the surface plasmon resonance.<sup>79,80</sup> Despite the arise of this background signal there appears to be significant counts close to the time delay of zero as shown with the inset in Figure 33. The decay of the background signal is very fast on the order of the instrument response, and the decay for the quantum dot at a time delay of zero has the very fast component, which resembles the background and a slower component as well. This slower component is suspected to be originate from multiexciton emission since it is not present in the background.

To overcome the large background counts, analysis of photon correlation data was done in several ways. The first method consisted of essentially time gating the fitted data. Assuming that everything  $\pm 2$  ns about the maxima of the peaks in the fits were largely

due to background, which appears to a valid assumption since upon fitting of the background signal time constants of several hundred picoseconds were measured, was excluded from calculations. Figure 36 shows how the side peak average lifetimes change in the presence of gold nanoparticles.

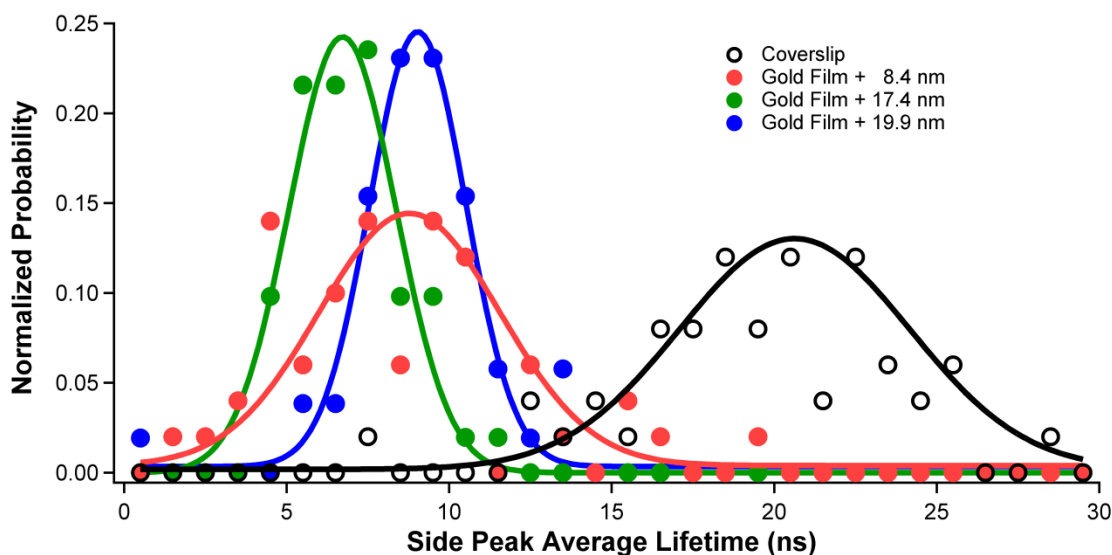


Figure 36: Side peak average lifetime in the presence of gold nanoparticles.

It can be seen that the shortest side peak average lifetimes were calculated at the 17.4 nm distance, which from analysis of blinking data is the distance suspected to have the largest plasmon-exciton interaction. Significant counts were also measured in the presence of gold particles at a time delay of zero, which gave rise to average lifetimes being calculated for the center peaks as well. Figure 37 demonstrates how the center peak average lifetimes change in the presence of gold nanoparticles.

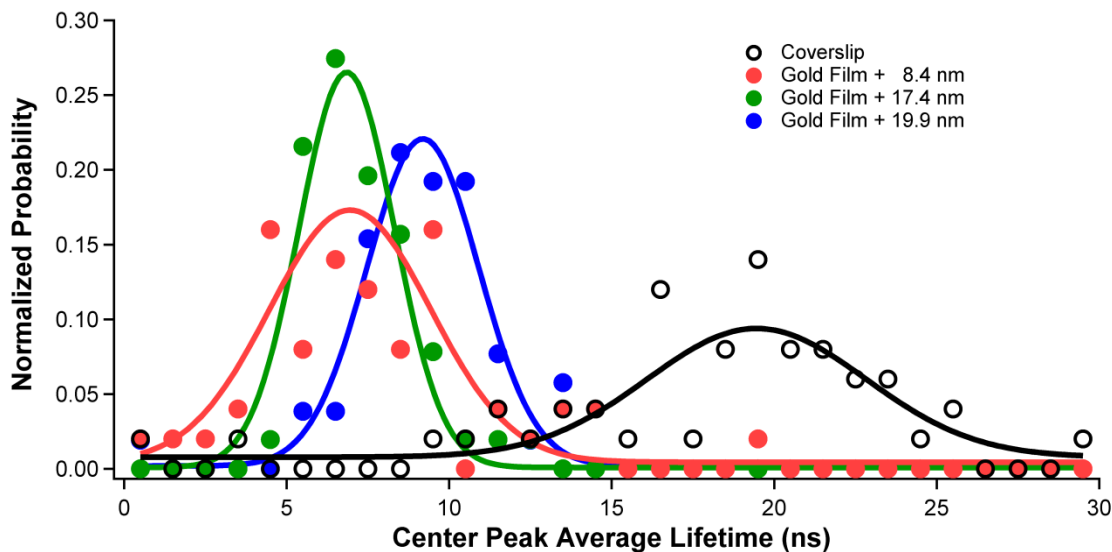


Figure 37: Center peak average lifetime in the presence of gold nanoparticles.

It is important to note that the average lifetimes measured from quantum dots on coverslip shown in Figure 37 arose from a few quantum dots. The probability of multiexciton emission is low, but can still occur from quantum dots on a coverslip. As seen in both Figure 36 and Figure 37 the average lifetimes for the side and center peaks decrease in the presence of gold nanoparticles. It should be noted that the average lifetime calculated for the center peak is not the average lifetime of the multiexciton. The counts in the center peak arise from two photons detected within the same pulse period, so this average lifetime is the time the single exciton took to emit relative to the biexciton. This suggests that lifetimes for the side and center peaks should be similar since the biexciton emission rate should be on the order of Auger recombination. As mentioned earlier a decrease in average lifetime alone is not adequate to describe the interaction occurring because the processes introduced by the gold particles (emission enhancement, multiexciton emission enhancement, and energy transfer) all result in a decrease of the average lifetime, however, it is important to note that the average lifetimes are always

shorter than a quantum dot on a coverslip especially when considering relative intensities (will be discussed later).

Nair et al. proposed that the ratio of the center peak to side peak areas is equal to the ratio of the biexciton to exciton quantum yields.<sup>17</sup> Here we use this ratio as a relative measure as Nair et al. reported their work was in the case of low excitation power where  $\langle N \rangle$  approaches zero, which was not done in this work.

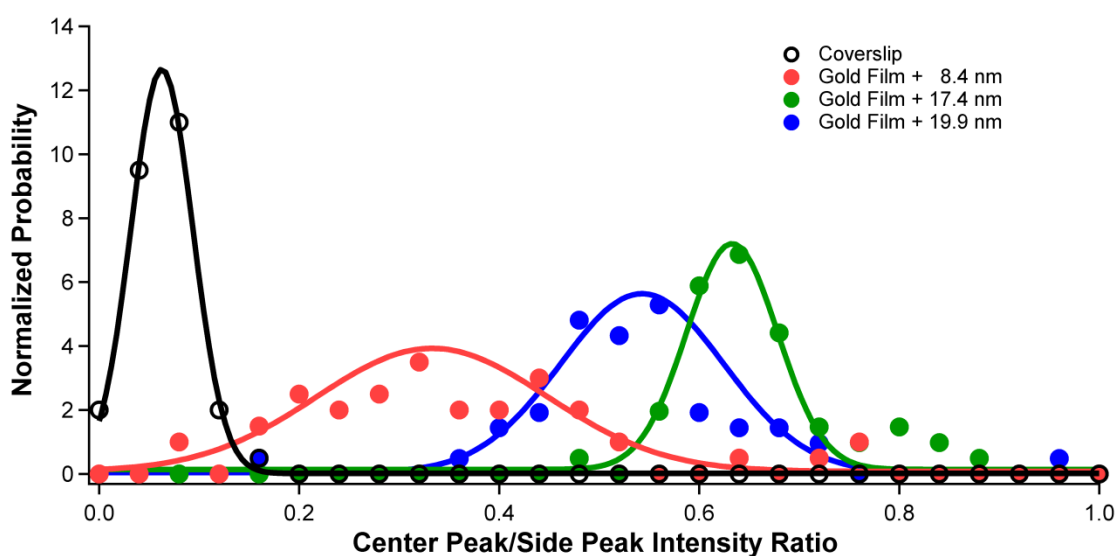


Figure 38: Center peak/side peak intensity ratio as a function of distance from gold

As mentioned the ratios of the center to side peak areas cannot be used to determine quantum yields of the biexciton state here, but the relative contributions of multiexciton emission to single exciton emission can be observed at a certain distance from gold nanoparticles as shown in Figure 38. For example at a spacer distance of 17.4 nm the intensity seen from multiexcitons is roughly equal to ~65% of the intensity seen from single exciton emission. This ratio also cannot be used to compare quantum dots from the different samples as that would assume the intensity from single exciton emission is the same for all distances, which is not the case as seen from the blinking analysis. Also

taking into account the competing energy transfer that is also distance-dependant and the possibility that the multiexciton emission rate doesn't change in the same way as the single exciton emission rate in the presence of gold these ratios could be misleading, and a clearer picture could actually be obtained from observing the changes in the side and center peak intensities separately.

Figure 39 shows the changes in the side peak intensities as the distance from gold is changed.

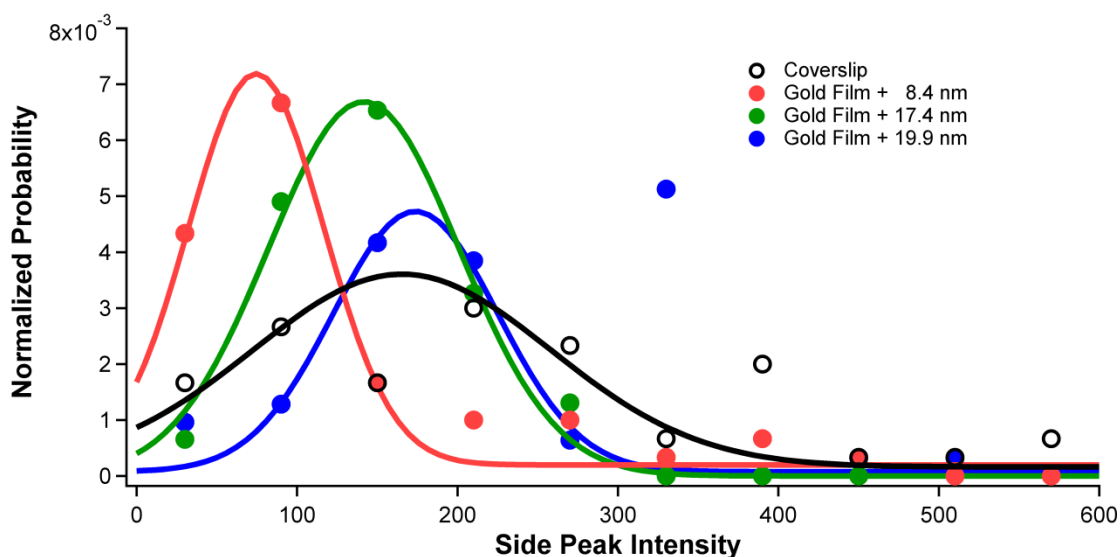


Figure 39: Side peak intensities in the presence of gold nanoparticles

The changes in side peak intensities in the presence of gold are in agreement with what was seen in the blinking analyses, where faster emission rates were measured in the presence of gold with the fastest rate measured at a 17.4 nm spacer distance indicating the strongest plasmon-exciton coupling strength. However, energy transfer is a competing process as well. Figure 39 suggest that the contributions from energy transfer may have been under estimated in the previous estimations from analyses of the blinking. At a 8.4 distance the intensity drops approximately by half, which is expected as energy transfer

would be the dominating process. At the farther distances the emission rate has been enhanced to a larger degree (measured shorter emission lifetimes) and energy transfer has decreased, but the overall effect from all the processes result in intensities being comparable to a quantum dot on a coverslip. Recall from Figure 36 the side peak average lifetimes were also shorter than a quantum dot on a coverslip, however at the 17.4 nm and 19.9 nm distances the intensity is comparable to a quantum dot on a coverslip. This further supports that the contribution from enhanced emission is more favorable compared to energy transfer, but energy transfer does contribute and the overall effect on peak intensity result in total intensities comparable to a quantum dot on a coverslip. Reviewing the blinking traces in the presence of gold and accounting for the increased background counts this trend was also demonstrated.

Figure 40 demonstrates the changes in the center peak intensities.

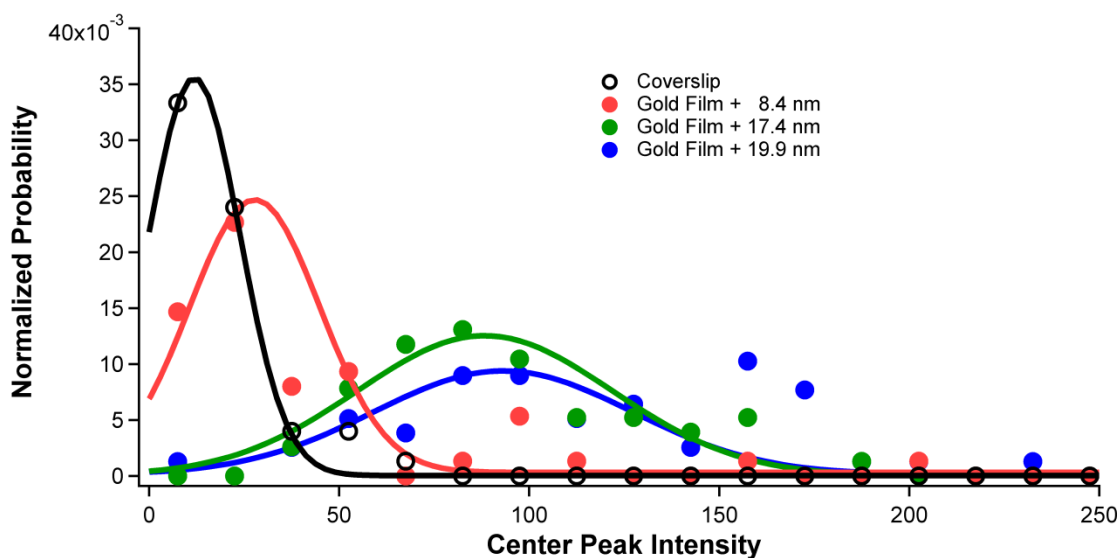


Figure 40: Center peak intensities in the presence of gold nanoparticles

As expected from Figure 40 quantum dots on a coverslip displayed almost no center peak intensity as Auger recombination is the dominating multiexciton decay channel.

However, in the presence of the gold nanoparticles the center peak intensities increase dramatically. An approximate 3-fold, 8-fold, and 9-fold increase in the intensity occur for the 8.4 nm, 17.4 nm, and 19.9 nm spacer distances respectively, which clearly indicates the multiexciton emission rate is also being enhanced in the presence of gold nanoparticles. The large increases in intensity could indicate that (a) the plasmon-multiexciton interactions is stronger than the plasmon-exciton interaction or (b) the energy transfer rate has less of an effect on multiexciton emission. Considering multiexciton emission is largely inhibited by Auger recombination, an increase in multiexciton emission intensity indicates that the multiexciton emission rate is now able to compete with the Auger recombination rate. This would lead to the expectation that the competing energy transfer (likely slower process than Auger recombination) process would have less of an effect on the multiexciton emission.<sup>81</sup> So enhancement of the multiexciton emission rate inferred by the increase in intensity also appears to be distance-dependant. However, further investigations are needed to determine the multiexciton emission lifetimes (rates) as current resources do not allow this ability.

The above analyses was done by ignoring the parts of the fitted data within  $\pm 2$  ns of the peak maximums. However, fitting is not perfect and subtle features can be missed. Also ignoring everything within the  $\pm 2$  ns time frame could also be removing contributions that truly originate from the quantum dot. In order to address these issues the analyses were repeated (except average lifetime determination), but on background corrected raw data. Photon correlation histograms were obtained for an area where no quantum dot was present for each sample and this histogram was considered as the contributions due to background. To produce background corrected photon correlation

histograms the background histogram at the maximum value at the zero time delay was normalized to the maximum value at the zero time delay in the quantum dot histogram. The normalized background histogram was then subtracted from the quantum dot histogram. Figure 41 shows uncorrected quantum dot and background histograms as well as the final corrected quantum dot histogram.

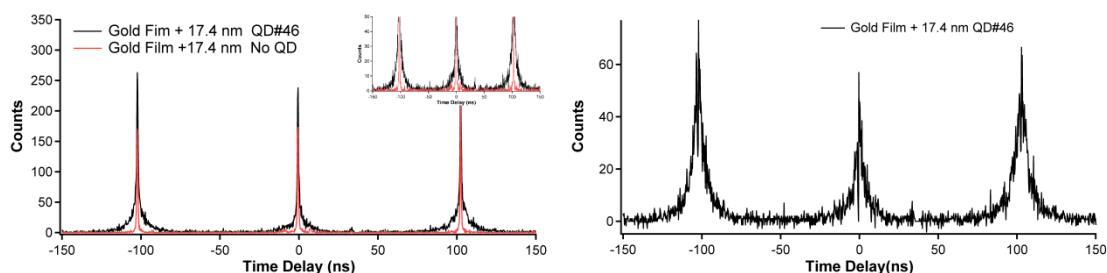


Figure 41: Original data and background (left) and background corrected data (right)

The normalization of the background and following subtraction was repeated for each quantum dot measured. Center peak to side peak ratios were then calculated as shown in Figure 42.

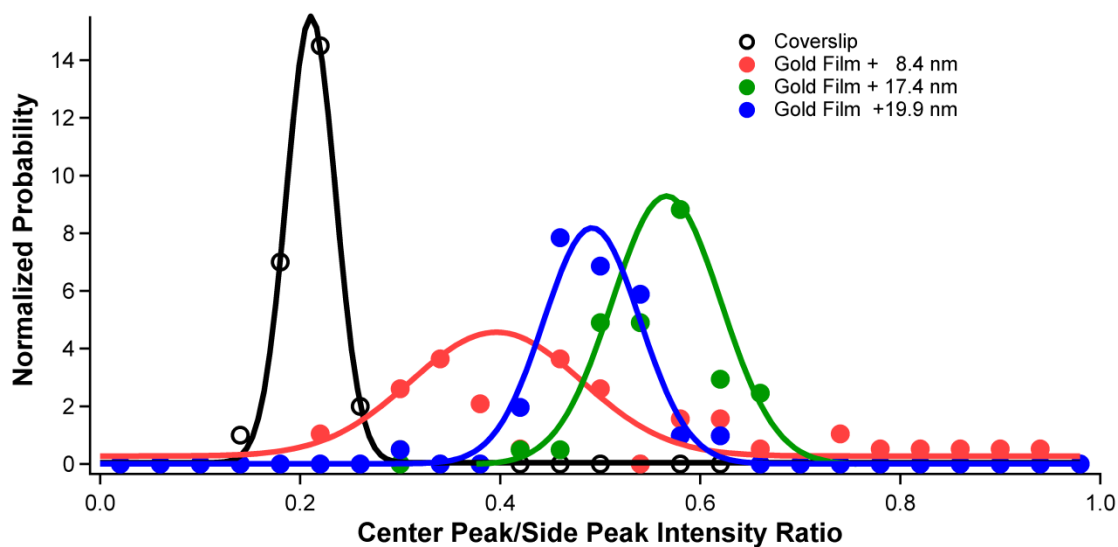


Figure 42: Background corrected center peak/side peak intensity ratios

Figure 42 demonstrates the same trend seen from the fitted data with slight differences in where the distributions occur. Corrected quantum dot correlation histograms also give a clearer illustration on changes seen at different distances from gold nanoparticles as shown in Figure 43.

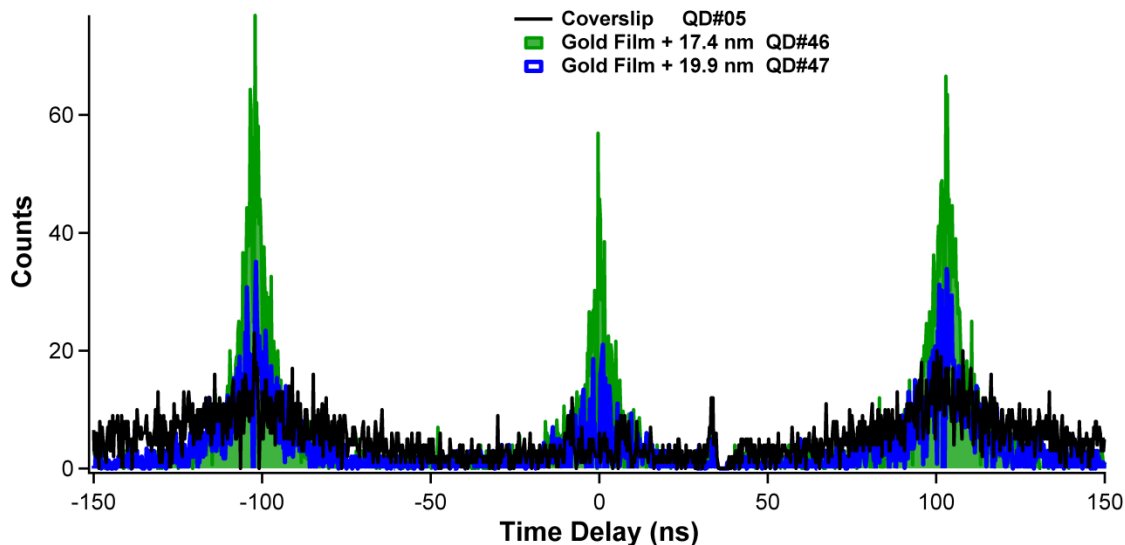


Figure 43: Background corrected photon correlation histograms near gold

The black trace in Figure 43 is showing how the decay of the side peaks occurs in the case with no gold present. Also seen is the lack of a significant peak at the zero time delay. However, in the presence of gold a center peak arises, indicating multiexciton emission. At the 17.4 nm distance the maximum of all three peaks (two side and one center) increases and decays rapidly relative to quantum dot on a coverslip. The effect of distance is also seen as the distance is increased to 19.9 nm the maximum of all peaks decreases and the decay rate decreases as well, but is still faster than the a quantum dot on a coverslip. The large changes seen for an approximate 3 nm difference clearly show how the interactions between the quantum and gold nanoparticles are strongly dependent on distance from each other. The increases in the peak maximums can be attributed to

enhancement of the multiexciton and exciton emission rates, but faster decays of the peaks would be expected if either the emission rates (exciton and multiexciton) were enhanced or energy transfer was occurring. More likely all three processes are occurring and the relative contributions shift based on the distance between the quantum dot and the gold nanoparticles. Side peak and center peak intensities were also calculated.

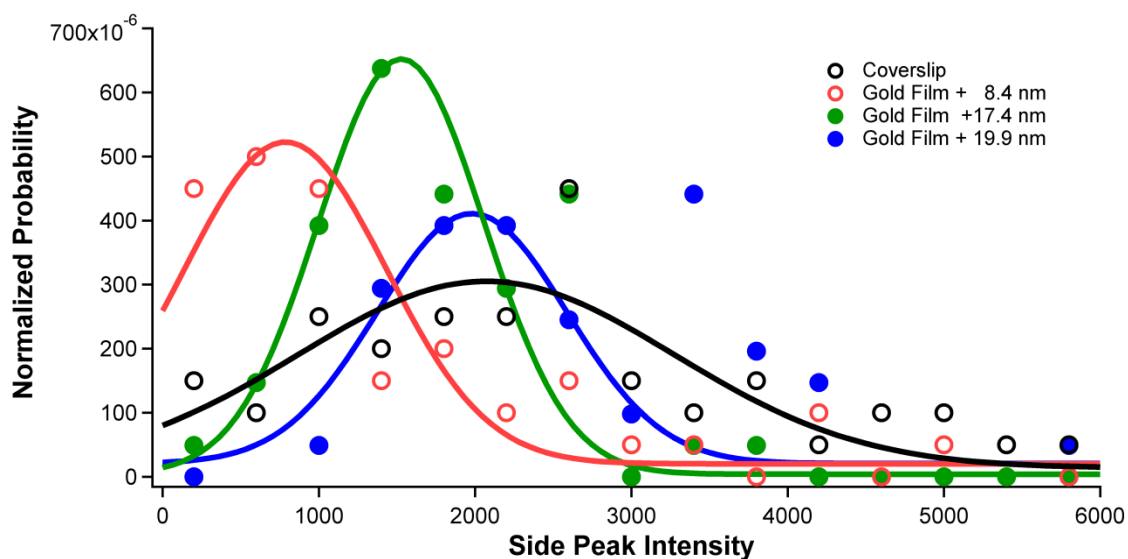


Figure 44: Background corrected side peak intensities

Figure 44 shows the side peak intensities calculated, which displays the same trend seen for the fitted data. Center peaks intensities were also calculated as shown in Figure 45, which again is in agreement for the trends seen for the fitted data as well.

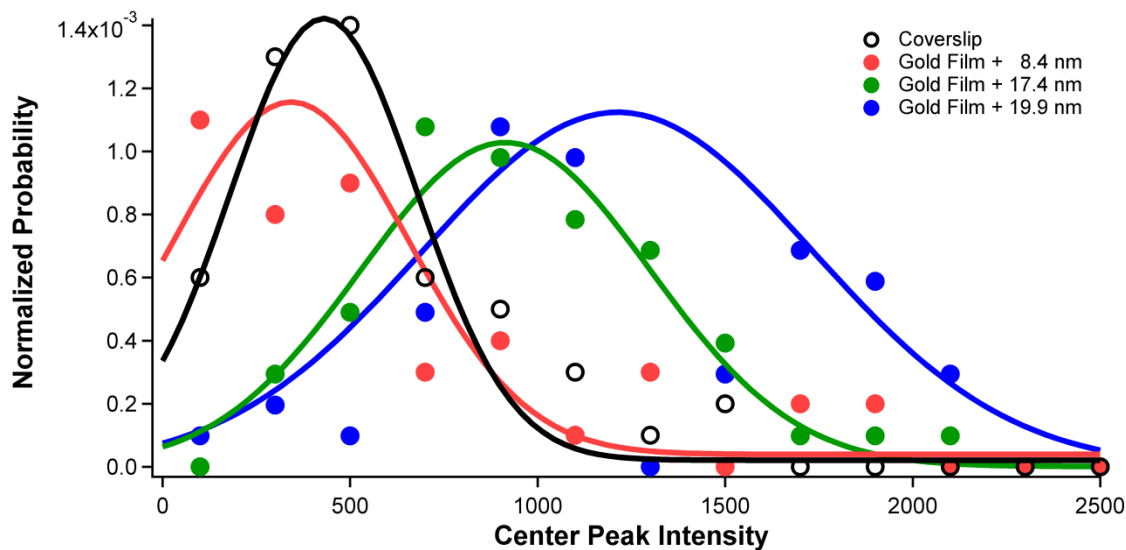


Figure 45: Background corrected center peak intensities

One deviation seen is in the center peak intensity of a quantum dot on a coverslip relative to the intensities for quantum dots in the presence of gold nanoparticles. The probability of a center peak arising for a quantum dot on just a coverslip is quite low due to Auger recombination and subtle features could be missed during the fitting process. However, center peak intensities obtained from the background corrected data of quantum dots could account for any subtle differences missed. Background correction of quantum dots on a coverslip were done in similar fashion to the correction done in the presence of gold. Collection of a photon correlation histogram was obtain on an area where no quantum dot was presence. The background signal seen on a coverslip appeared to be random noise, but the normalization and subtraction was still conducted so the treatment of all data was consistent.

## CHAPTER 5: CONCLUSIONS

The quantum dot and gold nanoparticle interaction was probed as a function of distance. High coverage gold nanoparticle films formed by bifunctional molecules displayed new surface plasmon modes due to particle-particle coupling. Deposition of polyelectrolytes displayed high controllability in uniform film thicknesses based on the number of layers deposited. Polyelectrolytes spacer layers also modified the surface plasmon resonance of the gold nanoparticle film, which resulted in an increase in intensity as well as a red shift. Completed gold/polyelectrolyte substrates demonstrated the modification of the emission properties of the CdSe/CdS quantum dots used in this study. It is suggested that the interaction between the two materials is quite complex consisting of a competition of processes. At the smallest distance studied of 8.4 nm non-radiative energy transfer dominates, which is supported by a decrease in emission counts and shorter average lifetimes seen in both blinking and photon correlations studies. At the 17.4 nm distance the plasmon-exciton interaction is the strongest for the distances studied. Supported by enhanced emission rates and suppression of blinking. At this distance photon correlation measurements determined relative multiexciton intensity to single exciton intensity ratios to be  $\sim 0.6$ . However, this relative measure could be a bit misleading when strictly looking at the multiexciton intensities and single exciton intensities separately as a function of distance. It is also suggested that non-radiative energy transfer is not fast enough to compete with the enhanced multiexciton emission

process, which would indicate that the multiexciton and exciton processes undergo different interactions. Lastly, these results demonstrate that the emission processes of the single and multiexciton states can be accurately controlled, which could be seen as useful routes in developing strategies for future applications such as light-emitting devices.

## REFERENCES

1. Shockley, W.; Queisser, H. J., DETAILED BALANCE LIMIT OF EFFICIENCY OF P-N JUNCTION SOLAR CELLS. *Journal of Applied Physics* **1961**, 32 (3), 510-&.
2. Hanna, M. C.; Nozik, A. J., Solar conversion efficiency of photovoltaic and photoelectrolysis cells with carrier multiplication absorbers. *Journal of Applied Physics* **2006**, 100 (7).
3. Nozik, A. J., SPECTROSCOPY AND HOT ELECTRON RELAXATION DYNAMICS IN SEMICONDUCTOR QUANTUM WELLS AND QUANTUM DOTS. *Annual Review of Physical Chemistry* **2001**, 52 (1), 193-231.
4. Alivisatos, A. P., Perspectives on the Physical Chemistry of Semiconductor Nanocrystals. *The Journal of Physical Chemistry* **1996**, 100 (31), 13226-13239.
5. Schaller, R. D.; Klimov, V. I., High efficiency carrier multiplication in PbSe nanocrystals: Implications for solar energy conversion. *Physical review letters* **2004**, 92 (18).
6. Sambur, J. B.; Novet, T.; Parkinson, B. A., Multiple Exciton Collection in a Sensitized Photovoltaic System. *Science* **2010**, 330 (6000), 63-66.
7. Klimov, V. I.; Mikhailovsky, A. A.; Xu, S.; Malko, A.; Hollingsworth, J. A.; Leatherdale, C. A.; Eisler, H.-J.; Bawendi, M. G., Optical Gain and Stimulated Emission in Nanocrystal Quantum Dots. *Science* **2000**, 290 (5490), 314-317.
8. Ivanov, S. A.; Nanda, J.; Piryatinski, A.; Achermann, M.; Balet, L. P.; Bezel, I. V.; Anikeeva, P. O.; Tretiak, S.; Klimov, V. I., Light Amplification Using Inverted Core/Shell Nanocrystals: Towards Lasing in the Single-Exciton Regime. *The Journal of Physical Chemistry B* **2004**, 108 (30), 10625-10630.
9. Klimov, V. I.; Ivanov, S. A.; Nanda, J.; Achermann, M.; Bezel, I.; McGuire, J. A.; Piryatinski, A., Single-exciton optical gain in semiconductor nanocrystals. *Nature* **2007**, 447 (7143), 441-446.
10. Nanda, J.; Ivanov, S. A.; Achermann, M.; Bezel, I.; Piryatinski, A.; Klimov, V. I., Light amplification in the single-exciton regime using exciton-exciton repulsion in type-II nanocrystal quantum dots. *Journal of Physical Chemistry C* **2007**, 111 (42), 15382-15390.
11. Kambhampati, P., Multiexcitons in Semiconductor Nanocrystals: A Platform for Optoelectronics at High Carrier Concentration. *The Journal of Physical Chemistry Letters* **2012**, 3 (9), 1182-1190.

12. Fisher, B.; Caruge, J. M.; Zehnder, D.; Bawendi, M., Room-Temperature Ordered Photon Emission from Multiexciton States in Single CdSe Core-Shell Nanocrystals. *Physical review letters* **2005**, *94* (8), 087403.
13. Stevenson, R. M.; Young, R. J.; Atkinson, P.; Cooper, K.; Ritchie, D. A.; Shields, A. J., A semiconductor source of triggered entangled photon pairs. *Nature* **2006**, *439* (7073), 179-182.
14. Shields, A. J., Semiconductor quantum light sources. *Nature Photonics* **2007**, *1* (4), 215-223.
15. Klimov, V. I., Mechanisms for photogeneration and recombination of multiexcitons in semiconductor nanocrystals: Implications for lasing and solar energy conversion. *Journal of Physical Chemistry B* **2006**, *110* (34), 16827-16845.
16. Htoon, H.; Malko, A. V.; Bussian, D.; Vela, J.; Chen, Y.; Hollingsworth, J. A.; Klimov, V. I., Highly Emissive Multiexcitons in Steady-State Photoluminescence of Individual "Giant" CdSe/CdS Core/Shell Nanocrystals. *Nano letters* **2010**, *10* (7), 2401-2407.
17. Nair, G.; Zhao, J.; Bawendi, M. G., Biexciton Quantum Yield of Single Semiconductor Nanocrystals from Photon Statistics. *Nano letters* **2011**, *11* (3), 1136-1140.
18. Park, Y. S.; Malko, A. V.; Vela, J.; Chen, Y.; Ghosh, Y.; García-Santamaría, F.; Hollingsworth, J. A.; Klimov, V. I.; Htoon, H., Near-Unity Quantum Yields of Biexciton Emission from CdSe/CdS Nanocrystals Measured Using Single-Particle Spectroscopy. *Physical review letters* **2011**, *106* (18), 187401.
19. Drexhage, K. H., INFLUENCE OF A DIELECTRIC INTERFACE ON FLUORESCENCE DECAY TIME. *Bulletin of the American Physical Society* **1969**, *14* (8), 873-&.
20. Ashcroft, N. W. M., N.D., *Solid State Physics*. Saunders College: Philadelphia, 1976.
21. Eustis, S.; El-Sayed, M. A., Why gold nanoparticles are more precious than pretty gold: Noble metal surface plasmon resonance and its enhancement of the radiative and nonradiative properties of nanocrystals of different shapes. *Chemical Society reviews* **2006**, *35* (3), 209-217.
22. Lakowicz, J. R., Radiative decay engineering 5: metal-enhanced fluorescence and plasmon emission. *Analytical Biochemistry* **2005**, *337* (2), 171-194.
23. Ma, X. D.; Tan, H.; Kipp, T.; Mews, A., Fluorescence Enhancement, Blinking Suppression, and Gray States of Individual Semiconductor Nanocrystals Close to Gold Nanoparticles. *Nano letters* **2010**, *10* (10), 4166-4174.

24. Gerber, S.; Reil, F.; Hohenester, U.; Schlagenhafen, T.; Krenn, J. R.; Leitner, A., Tailoring light emission properties of fluorophores by coupling to resonance-tuned metallic nanostructures. *Physical Review B* **2007**, *75* (7), 073404.
25. Kulakovich, O.; Strekal, N.; Yaroshevich, A.; Maskevich, S.; Gaponenko, S.; Nabiev, I.; Woggon, U.; Artemyev, M., Enhanced luminescence of CdSe quantum dots on gold colloids. *Nano letters* **2002**, *2* (12), 1449-1452.
26. Song, J. H.; Atay, T.; Shi, S. F.; Urabe, H.; Nurmikko, A. V., Large enhancement of fluorescence efficiency from CdSe/ZnS quantum dots induced by resonant coupling to spatially controlled surface plasmons. *Nano letters* **2005**, *5* (8), 1557-1561.
27. Okamoto, K.; Vyawahare, S.; Scherer, A., Surface-plasmon enhanced bright emission from CdSe quantum-dot nanocrystals. *Journal of the Optical Society of America B-Optical Physics* **2006**, *23* (8), 1674-1678.
28. Pompa, P. P.; Martiradonna, L.; Della Torre, A.; Della Sala, F.; Manna, L.; De Vittorio, M.; Calabi, F.; Cingolani, R.; Rinaldi, R., Metal-enhanced fluorescence of colloidal nanocrystals with nanoscale control. *Nature nanotechnology* **2006**, *1* (2), 126-130.
29. Fedutik, Y.; Temnov, V. V.; Schops, O.; Woggon, U.; Artemyev, M. V., Exciton-plasmon-photon conversion in plasmonic nanostructures. *Physical review letters* **2007**, *99* (13).
30. Ito, Y.; Matsuda, K.; Kanemitsu, Y., Mechanism of photoluminescence enhancement in single semiconductor nanocrystals on metal surfaces. *Physical Review B* **2007**, *75* (3), 033309.
31. Munechika, K.; Chen, Y.; Tillack, A. F.; Kulkarni, A. P.; Plante, I. J.-L.; Munro, A. M.; Ginger, D. S., Spectral Control of Plasmonic Emission Enhancement from Quantum Dots near Single Silver Nanoprisms. *Nano letters* **2010**, *10* (7), 2598-2603.
32. Lakowicz, J. R.; Ray, K.; Chowdhury, M.; Szymanski, H.; Fu, Y.; Zhang, J.; Nowaczyk, K., Plasmon-controlled fluorescence: a new paradigm in fluorescence spectroscopy. *The Analyst* **2008**, *133* (10), 1308-1346.
33. Purcell, E. M., SPONTANEOUS EMISSION PROBABILITIES AT RADIO FREQUENCIES. *Physical Review* **1946**, *69* (11-1), 681-681.
34. Nirmal, M.; Dabbousi, B. O.; Bawendi, M. G.; Macklin, J. J.; Trautman, J. K.; Harris, T. D.; Brus, L. E., Fluorescence intermittency in single cadmium selenide nanocrystals. *Nature* **1996**, *383* (6603), 802-804.
35. Efros, A. L.; Rosen, M., Random telegraph signal in the photoluminescence intensity of a single quantum dot. *Physical review letters* **1997**, *78* (6), 1110-1113.

36. Masuo, S.; Naiki, H.; Machida, S.; Itaya, A., Photon statistics in enhanced fluorescence from a single CdSe/ZnS quantum dot in the vicinity of silver nanoparticles. *Applied physics letters* **2009**, *95* (19), 193106.
37. LeBlanc, S. J.; McClanahan, M. R.; Jones, M.; Moyer, P. J., Enhancement of Multiphoton Emission from Single CdSe Quantum Dots Coupled to Gold Films. *Nano letters* **2013**, *13* (4), 1662-1669.
38. Aroca, R.; Kovacs, G. J.; Jennings, C. A.; Loutfy, R. O.; Vincett, P. S., FLUORESCENCE ENHANCEMENT FROM LANGMUIR-BLODGETT MONOLAYERS ON SILVER ISLAND FILMS. *Langmuir : the ACS journal of surfaces and colloids* **1988**, *4* (3), 518-521.
39. Thomas, K. G.; Kamat, P. V., Chromophore-functionalized gold nanoparticles. *Accounts of Chemical Research* **2003**, *36* (12), 888-898.
40. Lakowicz, J. R.; Geddes, C. D.; Gryczynski, I.; Malicka, J.; Gryczynski, Z.; Aslan, K.; Lukomska, J.; Matveeva, E.; Zhang, J. A.; Badugu, R.; Huang, J., Advances in surface-enhanced fluorescence. *Journal of Fluorescence* **2004**, *14* (4), 425-441.
41. Lakowicz, J. R.; Chowdhury, M. H.; Ray, K.; Zhang, J.; Fu, Y.; Badugu, R.; Sabanayagam, C. R.; Nowaczyk, K.; Szmecinski, H.; Aslan, K.; Geddes, C. D., Plasmon-controlled fluorescence: A new detection technology - art. no. 609909. In *Plasmonics in Biology and Medicine III*, Tuan, V.; Lakowicz, J. R.; Gryczynski, Z., Eds. Spie-Int Soc Optical Engineering: Bellingham, 2006; Vol. 6099, pp 9909-9909.
42. Matsuda, K.; Ito, Y.; Kanemitsu, Y., Photoluminescence enhancement and quenching of single CdSe/ZnS nanocrystals on metal surfaces dominated by plasmon resonant energy transfer. *Applied physics letters* **2008**, *92* (21).
43. Naiki, H.; Masuo, S.; Machida, S.; Itaya, A., Single-Photon Emission Behavior of Isolated CdSe/ZnS Quantum Dots Interacting with the Localized Surface Plasmon Resonance of Silver Nanoparticles. *Journal of Physical Chemistry C* **2011**, *115* (47), 23299-23304.
44. Freeman, R. G.; Grabar, K. C.; Allison, K. J.; Bright, R. M.; Davis, J. A.; Guthrie, A. P.; Hommer, M. B.; Jackson, M. A.; Smith, P. C.; Walter, D. G.; Natan, M. J., SELF-ASSEMBLED METAL COLLOID MONOLAYERS - AN APPROACH TO SERS SUBSTRATES. *Science* **1995**, *267* (5204), 1629-1632.
45. Grabar, K. C.; Freeman, R. G.; Hommer, M. B.; Natan, M. J., PREPARATION AND CHARACTERIZATION OF AU COLLOID MONOLAYERS. *Analytical Chemistry* **1995**, *67* (4), 735-743.
46. Grabar, K. C.; Allison, K. J.; Baker, B. E.; Bright, R. M.; Brown, K. R.; Freeman, R. G.; Fox, A. P.; Keating, C. D.; Musick, M. D.; Natan, M. J., Two-dimensional arrays of colloidal gold particles: A flexible approach to macroscopic metal surfaces. *Langmuir : the ACS journal of surfaces and colloids* **1996**, *12* (10), 2353-2361.

47. Grabar, K. C.; Smith, P. C.; Musick, M. D.; Davis, J. A.; Walter, D. G.; Jackson, M. A.; Guthrie, A. P.; Natan, M. J., Kinetic control of interparticle spacing in Au colloid-based surfaces: Rational nanometer-scale architecture. *Journal of the American Chemical Society* **1996**, *118* (5), 1148-1153.
48. Tseng, J. Y.; Lin, M. H.; Chau, L. K., Preparation of colloidal gold multilayers with 3-(mercaptopropyl)-trimethoxysilane as a linker molecule. *Colloids and Surfaces a-Physicochemical and Engineering Aspects* **2001**, *182* (1-3), 239-245.
49. Mulvaney, S. P.; He, L.; Natan, M. J.; Keating, C. D., Three-layer substrates for surface-enhanced Raman scattering: preparation and preliminary evaluation. *Journal of Raman Spectroscopy* **2003**, *34* (2), 163-171.
50. Musick, M. D.; Keating, C. D.; Keefe, M. H.; Natan, M. J., Stepwise construction of conductive Au colloid multilayers from solution. *Chemistry of Materials* **1997**, *9* (7), 1499-&.
51. Musick, M. D.; Pena, D. J.; Botsko, S. L.; McEvoy, T. M.; Richardson, J. N.; Natan, M. J., Electrochemical properties of colloidal Au-based surfaces: Multilayer assemblies and seeded colloid films. *Langmuir : the ACS journal of surfaces and colloids* **1999**, *15* (3), 844-850.
52. Turkevich, J.; Stevenson, P. C.; Hillier, J., A study of the nucleation and growth processes in the synthesis of colloidal gold. *Discussions of the Faraday Society* **1951**, *11* (0), 55-75.
53. Turkevich, J.; Stevenson, P. C.; Hillier, J., THE FORMATION OF COLLOIDAL GOLD. *Journal of Physical Chemistry* **1953**, *57* (7), 670-673.
54. Caruso, F., Nanoengineering of Particle Surfaces. *Advanced materials* **2001**, *13* (1), 11-22.
55. Caruso, F.; Niikura, K.; Furlong, D. N.; Okahata, Y., Ultrathin multilayer polyelectrolyte films on gold: Construction and thickness determination .1. *Langmuir : the ACS journal of surfaces and colloids* **1997**, *13* (13), 3422-3426.
56. Gittins, D. I.; Caruso, F., Tailoring the Polyelectrolyte Coating of Metal Nanoparticles. *The Journal of Physical Chemistry B* **2001**, *105* (29), 6846-6852.
57. Schneider, G.; Decher, G., From functional core/shell nanoparticles prepared via layer-by-layer deposition to empty nanospheres. *Nano letters* **2004**, *4* (10), 1833-1839.
58. Schneider, G.; Decher, G., Functional core/shell nanoparticles via layer-by-layer assembly. investigation of the experimental parameters for controlling particle aggregation and for enhancing dispersion stability. *Langmuir : the ACS journal of surfaces and colloids* **2008**, *24* (5), 1778-1789.

59. Jin, Y. D.; Gao, X. H., Plasmonic fluorescent quantum dots. *Nature nanotechnology* **2009**, *4* (9), 571-576.
60. Lvov, Y.; Decher, G.; Moehwald, H., Assembly, structural characterization, and thermal behavior of layer-by-layer deposited ultrathin films of poly(vinyl sulfate) and poly(allylamine). *Langmuir : the ACS journal of surfaces and colloids* **1993**, *9* (2), 481-486.
61. Decher, G., Fuzzy nanoassemblies: Toward layered polymeric multicomposites. *Science* **1997**, *277* (5330), 1232-1237.
62. Caruso, F.; Lichtenfeld, H.; Donath, E.; Mohwald, H., Investigation of electrostatic interactions in polyelectrolyte multilayer films: Binding of anionic fluorescent probes to layers assembled onto colloids. *Macromolecules* **1999**, *32* (7), 2317-2328.
63. Dubas, S. T.; Schlenoff, J. B., Factors controlling the growth of polyelectrolyte multilayers. *Macromolecules* **1999**, *32* (24), 8153-8160.
64. Schlenoff, J. B.; Dubas, S. T., Mechanism of polyelectrolyte multilayer growth: Charge overcompensation and distribution. *Macromolecules* **2001**, *34* (3), 592-598.
65. Cho, J.; Char, K.; Hong, J. D.; Lee, K. B., Fabrication of highly ordered multilayer films using a spin self-assembly method. *Advanced materials* **2001**, *13* (14), 1076-+.
66. Chiarelli, P. A.; Johal, M. S.; Casson, J. L.; Roberts, J. B.; Robinson, J. M.; Wang, H. L., Controlled fabrication of polyelectrolyte multilayer thin films using spin-assembly. *Advanced materials* **2001**, *13* (15), 1167-+.
67. Chiarelli, P. A.; Johal, M. S.; Holmes, D. J.; Casson, J. L.; Robinson, J. M.; Wang, H. L., Polyelectrolyte spin-assembly. *Langmuir : the ACS journal of surfaces and colloids* **2002**, *18* (1), 168-173.
68. Jiang, C. Y.; Markutsya, S.; Tsukruk, V. V., Collective and individual plasmon resonances in nanoparticle films obtained by spin-assisted layer-by-layer assembly. *Langmuir : the ACS journal of surfaces and colloids* **2004**, *20* (3), 882-890.
69. Lefaux, C. J.; Zimberlin, J. A.; Dobrynin, A. V.; Mather, P. T., Polyelectrolyte spin assembly: Influence of ionic strength on the growth of multilayered thin films. *Journal of Polymer Science Part B-Polymer Physics* **2004**, *42* (19), 3654-3666.
70. Haiss, W.; Thanh, N. T. K.; Aveyard, J.; Fernig, D. G., Determination of size and concentration of gold nanoparticles from UV-Vis spectra. *Analytical Chemistry* **2007**, *79* (11), 4215-4221.
71. Schneider, C. A.; Rasband, W. S.; Eliceiri, K. W., NIH Image to ImageJ: 25 years of image analysis. *Nature methods* **2012**, *9* (7), 671-675.

72. Brown, R. H.; Twiss, R. Q., Correlation between Photons in two Coherent Beams of Light. *Nature* **1956**, *177* (4497), 27-29.
73. Keating, C. D.; Musick, M. D.; Keefe, M. H.; Natan, M. J., Kinetics and Thermodynamics of Au Colloid Monolayer Self-Assembly: Undergraduate Experiments in Surface and Nanomaterials Chemistry. *Journal of Chemical Education* **1999**, *76* (7), 949.
74. Jiang, C.; Markutsya, S.; Tsukruk, V. V., Collective and Individual Plasmon Resonances in Nanoparticle Films Obtained by Spin-Assisted Layer-by-Layer Assembly. *Langmuir : the ACS journal of surfaces and colloids* **2003**, *20* (3), 882-890.
75. Albrecht, C., Joseph R. Lakowicz: Principles of fluorescence spectroscopy, 3rd Edition. *Analytical and Bioanalytical Chemistry* **2008**, *390* (5), 1223-1224.
76. Zhao, J.; Chen, O.; Strasfeld, D. B.; Bawendi, M. G., Biexciton Quantum Yield Heterogeneities in Single CdSe (CdS) Core (Shell) Nanocrystals and Its Correlation to Exciton Blinking. *Nano letters* **2012**, *12* (9), 4477-4483.
77. Fisher, B. R.; Eisler, H.-J.; Stott, N. E.; Bawendi, M. G., Emission Intensity Dependence and Single-Exponential Behavior In Single Colloidal Quantum Dot Fluorescence Lifetimes. *The Journal of Physical Chemistry B* **2003**, *108* (1), 143-148.
78. Wu, X.; Sun, Y.; Pelton, M., Recombination rates for single colloidal quantum dots near a smooth metal film. *Physical Chemistry Chemical Physics* **2009**, *11* (28), 5867-5870.
79. Geddes, C. D.; Parfenov, A.; Gryczynski, I.; Lakowicz, J. R., Luminescent blinking of gold nanoparticles. *Chemical physics letters* **2003**, *380* (3-4), 269-272.
80. Dulkeith, E.; Niedereichholz, T.; Klar, T.; Feldmann, J.; von Plessen, G.; Gittins, D.; Mayya, K.; Caruso, F., Plasmon emission in photoexcited gold nanoparticles. *Physical Review B* **2004**, *70* (20), 205424.
81. Cheng, H.-W.; Yuan, C.-T.; Wang, J.-S.; Lin, T.-N.; Shen, J.-L.; Hung, Y.-J.; Tang, J.; Tseng, F.-G., Modification of Photon Emission Statistics from Single Colloidal CdSe Quantum Dots by Conductive Materials. *The Journal of Physical Chemistry C* **2014**, *118* (31), 18126-18132.